# Structure of the human CTF18–RFC clamp loader bound to PCNA

Giuseppina R. Briola[1¶], Muhammad Tehseen[1¶], Amani Al-Amodi[1], Grace Young[2], Ammar U. Danazumi[1], Phong Quoc Nguyen[1], Christos G. Savva[1], Mark Hedglin[2], Samir M. Hamdan[1,3*] and Alfredo De Biasio[1*]

[1]Bioscience Program, Division of Biological and Environmental Sciences and Engineering, King Abdullah University of Science and Technology, Thuwal 23955, Saudi Arabia.

[2]Department of Chemistry, The Pennsylvania State University, University Park, PA, USA 16802

[3]KAUST Center of Excellence for Smart Health, King Abdullah University of Science and Technology, Thuwal 23955, Saudi Arabia.

*Corresponding authors

E-mail: samir.hamdan@kaust.edu.sa or alfredo.debiasio@kaust.edu.sa

[¶]These authors contributed equally to this work.

# Abstract

Sliding clamps like PCNA are crucial processivity factors for replicative polymerases, requiring specific clamp loaders for loading onto DNA. The human alternative clamp loader CTF18-RFC interacts with the leading strand polymerase Pol ε and loads PCNA onto primer/template DNA using its RFC pentameric module. Here, we provide a structural characterization of the human CTF18-RFC complex and its interaction with PCNA. Our cryo-EM data support that the Ctf8 and Dcc1 subunits of CTF18-RFC, which form the regulatory module interacting with Pol ε, are flexibly tethered to the RFC module. A 2.9 Å cryo-EM structure shows the RFC module bound to PCNA in an auto-inhibited conformation similar to the canonical RFC loader, marking the initial step of the clamp-loading reaction. The unique RFC1 (Ctf18) large subunit of CTF18-RFC, which based on the cryo-EM map shows high relative flexibility, is anchored to PCNA through an atypical low-affinity PIP box in the AAA+ domain and engages the RFC5 subunit using a novel β-hairpin at the disordered N-terminus. We show that deletion of this β-hairpin impairs the CTF18-RFC–PCNA complex stability, slows down clamp loading, and decreases the rate of primer synthesis by Pol ε. Our research identifies distinctive structural characteristics of the human CTF18-RFC complex, providing insights into its role in PCNA loading and the stimulation of leading strand synthesis by Pol ε.


# Introduction

High fidelity and efficiency are critical for chromosomal DNA duplication in eukaryotes. This precision is achieved through the coordinated action of replicative DNA

polymerases, Pol δ and Pol ε, anchored to the sliding clamp, Proliferating Cell Nuclear Antigen (PCNA) (1). The ring-shaped PCNA homotrimer encircles DNA, enhancing the processivity of these polymerases in DNA replication and repair processes, including excision repair and homologous recombination (2), and plays an important role in sister chromatid cohesion establishment (3). The closed-ring topology of PCNA necessitates the transient opening of one interface to facilitate the incorporation and trapping of primer-template DNA. This critical function is executed by pentameric AAA+ (ATPases Associated with diverse cellular Activities) ATPases, collectively known as clamp loaders (4-6). Extensive structural and biochemical work in different organisms (7-12) established a common mechanism for the clamp-loading reaction, which proceeds through three main steps (13-18). Initially, the clamp loader engages with the intact clamp ring, adopting an autoinhibited configuration that precludes DNA binding (10). This stage sets the groundwork for the subsequent transition, where the clamp loader alters its conformation to an activated state. This change facilitates the opening of the clamp ring, creating a gap sufficiently large to permit the passage of duplex DNA and aligning the clamp loader for primer-template DNA interaction. The final phase of this process is initiated by the binding of DNA to the clamp loader, catalysing ATP hydrolysis. DNA binding prompts the closure of the clamp and hydrolysis of ATP induces the concurrent disassembly of the closed clamp loader from the sliding clamp-DNA complex, completing the cycle necessary for the engagement of the replicative polymerases to start DNA synthesis.

The canonical Replication Factor C (RFC), consisting of a large RFC1 subunit and four subunits (RFC2, RFC3, RFC4, and RFC5), acts as the primary clamp loader

for PCNA (4), (19). However, eukaryotes also employ alternative loaders (20), including CTF18-RFC (6), (21-24), which likely use a conserved loading mechanism but are functionally specialized through specific protein interactions and context-dependent roles in DNA replication.

Genome-wide analyses revealed that CTF18-RFC predominantly facilitates PCNA loading on the leading strand, in contrast to the canonical RFC complex, which mainly loads PCNA on the lagging strand (25). Although CTF18-RFC is not essential for bulk DNA replication in yeast (26, 27), it plays a vital role in ensuring sister chromatid cohesion (21), (28, 29). This may be due to its selective loading of PCNA linked to EcoI acetyltransferase (3), which acetylates Smc3, preventing cohesin destabilization by WapI (30-32). Recruitment of CTF18-RFC to the leading strand is also important for activation of the replication checkpoint (22) (24) (33, 34).

The CTF18-RFC complex features two distinct modules with separate functions (23), (28, 35, 36): a catalytic RFC module for PCNA loading, consisting of a large RFC1-like subunit (hereby referred to as Ctf18), alongside the four RFC2, RFC3, RFC4 and RFC5 subunits utilized by the canonical RFC complex, and a regulatory module, made up of the Ctf8 and Dcc1 subunits. These latter two subunits attach to the Ctf18 C-terminus, forming the Ctf18-1-8 module. A long linker predicted to be flexible connects these two segments (34) (37). Structural and functional studies have demonstrated that the interaction between the Ctf18-1-8 module and the catalytic domain of Pol2 ($Pol2_{CAT}$), the principal subunit of Pol ε, directs CTF18-RFC to replication forks and boosts its clamp loading efficiency (34) (37). This interaction situates the clamp loader close to the primer/template junction, facilitating PCNA loading (34). $Pol2_{CAT}$ is tethered to the

remainder of Pol ε via an unstructured linker, making it an integral component of the CMGE (Cdc45-Mcm-GINS-Pol ε) core replisome complex (38). It has been proposed that Pol ε utilizes both the CMG helicase and PCNA as processivity factors to facilitate normal replication rates (39) (40). Tethering by the CMG complex might allow Pol ε to dissociate from the 3′ end of the leading strand but stay at the replication fork until leading strand synthesis restarts. Given the relatively weak interaction of Pol ε with PCNA (41), it is possible that multiple PCNA loading events on the leading strand via CTF18-RFC are necessary to achieve full Pol ε processivity.

Although the structure of the Ctf18-1-8 module in association with $Pol2_{CAT}$ has been elucidated (34) (37), the architecture of the CTF18-RFC module and its interaction with PCNA remain uncharacterized. To investigate the clamp loading mechanism employed by CTF18-RFC, we reconstituted the full human CTF18-RFC complex with PCNA and determined its structure using cryo-electron microscopy (cryo-EM). Our cryo-EM data supports the prediction that the Ctf18-1-8 and RFC modules are flexibly tethered. The analysis yielded high-resolution reconstructions of the entire CTF18-RFC module bound to a closed PCNA ring. Although the overall architecture mirrors the autoinhibited state observed in the canonical RFC loader in a complex with PCNA (10), distinctive features within CTF18-RFC were identified. These distinctions may offer insights into the specialized functional roles CTF18-RFC plays in DNA replication.

# Results

## Structure of the human CTF18-RFC–PCNA complex

We employed single-particle cryo-EM to determine the structure of human CTF18-RFCbound to PCNA. To this purpose, the full CTF18-RFC complex, including Ctf8 and Dcc1, was expressed in insect cells and purified to homogeneity (Fig S1). The purified complex includes all subunits as shown in the SDS-PAGE gel (Fig S1). With the aim of trapping CTF18-RFCin different steps of the clamp loading reaction, the complex was vitrified in the presence of ATP, PCNA, and primer/template DNA but omitting the $Mg^{2+}$ cofactor to halt hydrolysis (42), and then imaged by cryo-EM (Fig S2). Surprisingly, image processing yielded only a major 3D class, including the CTF18-RFC pentamer bound to a closed PCNA ring (Fig 1a-b, Fig S2-3), with no evidence of DNA density. The Ctf18-1-8 module, which is connected to the RFC module by a 91 amino acid linker (Fig 1a), is not resolved in the map (Fig 1b), suggesting it is flexibly tethered to the RFC module. The map was refined to a global resolution of 2.9 Å (Fig S2-3), which allowed model building of the five CTF18-RFC subunits as well as the PCNA homotrimer (Fig 1c). The final model refines to a map-to-model FSC of 3.0 Å at 0.5 threshold, with good refinement statistics (S1 Table).

The five CTF18-RFC subunits are positioned on top of the closed PCNA ring, which is planar and undistorted (Fig 1c). A structural comparison shows that the CTF18-RFC pentamer was trapped in an autoinhibited conformation analogous to that reported for the canonical human (h) and yeast (sc) RFC (8), (10), pertaining to the initial step of the clamp loading reaction, right before clamp opening (Fig 1d). In such conformation, the AAA+ domains form an overtwisted and asymmetric spiral that is incompatible with DNA binding (8), (10). The AAA+, collar, and A' domains of the Ctf18 subunit (Fig 2a) align with the homologous domains of hRFC1 (Fig 2b). As in the hRFC structure (10),

the Ctf18 subunit interacts with RFC2, RFC3, and PCNA-I. Three main deviations from the hRFC–PCNA structure are observed (10): a different tilt of the PCNA ring (Fig 1c-d), significant mobility of the large Ctf18 subunit (Fig 1b and Fig S2) and, importantly, the presence of a β-hairpin engaged to the outer surface of the RFC5 subunit, which we mapped to the disordered N-terminus of the Ctf18 subunit (Fig 2a and 2c). These features are analyzed in detail below.

## Structure of the large subunit of CTF18-RFC

The Ctf18 subunit presents 26% identity with the homologous subunit RFC1 of hRFC and an overall structural conservation, with some deviations particularly in the A' domain (Fig 2b). Compared to the other subunits, the AAA+ domain of Ctf18 shows increased flexibility, as evidenced by the local resolution map of the complex as well as 3D variability analysis (43) (44) (Fig S2d and Supplementary Video 1). Increased flexibility was not detected in the RFC1 subunit of human RFC bound to PCNA (10). This discrepancy could be explained by diminished inter-subunit interactions involving both the AAA+ and collar domains of Ctf18 compared to RFC1, as illustrated in Fig S4: the AAA+ domain of Ctf18 forms fewer stabilizing salt bridges and h-bonds with RFC2 than RFC1 does, and the Ctf18 collar domain establishes markedly weaker interactions with both RFC2 and RFC3 than the extensive network observed for RFC1. Conversely, the interaction between the A' domain of CTF18-RFC and RFC3 is strong as observed for RFC. Overall, the total buried surface area between Ctf18 and interacting subunits is comparable to that of RFC1 (~5500 Å$^2$ versus ~5300 Å$^2$). However, the buried surface area between Ctf18 and RFC2 is markedly smaller than that of RFC1 (~1400 Å$^2$ and ~2300 Å$^2$). As explained below, the lost interactions mediated by the AAA+ and collar

domains of Ctf18 are partially counterbalanced by those established with the N-terminal β-hairpin, which is absent in the canonical RFC. Additionally, the interaction between Ctf18 and PCNA is weaker compared to the interaction between RFC1 and PCNA, further contributing to these structural differences (see next section). The Ctf18 C-terminal region (residues 953-975) predicted to interact with the Ctf8 and Dcc1 subunits (Fig 2a) is invisible in the map.

The most striking feature is a small β-hairpin-containing fold mapped between residues 165-194 in the disordered N-terminus (Fig 2a and 2c) of the Ctf18 subunit, ~80 Å apart from the Ctf18 AAA+ domain, to which it is connected by a disordered linker of 86 amino acids (residues 195-280). This N-terminal fold plugs into a groove at the outer surface of the collar domain of the RFC5 subunit defined by helices α1, α3, α4, and α5 (Fig 3a). The resolution of the map in this region is sufficient for confident model building of the interface (Fig 3b). The interface buries 984 $Å^2$ and is characterized by both apolar and polar interactions (Fig 3a). A set of hydrophobic side chains protruding from Ctf18 β-hairpin (V178, V180, L190, L192) approaches a complementary patch of hydrophobic residues on RFC5 (L255 in α1; F287, V291 and F293 in α3; I336 and V337 in α5). The interface is further strengthened by several hydrogen bonds mostly mediated by main-chain atoms in the Ctf18 β-hairpin, and by a salt bridge between R193 of the Ctf18 β-hairpin and D292 of RFC5. It is worth highlighting that RFC2 separates the Ctf18 and RFC5 subunits. Despite this separation, Ctf18 projects the β-hairpin directly onto RFC5, bypassing any interactions with RFC2 (Fig 2c). This observation supports that the β-hairpin functions as a “latch” to stabilize the CTF18-RFC structure.

Similarly to human CTF18-RFC, long regions predicted to be disordered by AlphaFold (45) are present in the N-terminal sequence of Ctf18 of lower eukaryotes. The β-hairpin region of human Ctf18 does not show strict sequence conservation, but a similar fold in the N-terminus of lower eukaryotes Ctf18 is predicted (Fig 2a). Therefore, lower eukaryotes may use a similar β-hairpin motif to bind the corresponding subunit of the RFC-module complex (RFC5 in human, Rfc3 in *S. cerevisiae)*, emphasizing its importance.

## Interactions of CTF18-RFC with PCNA

CTF18-RFC engages two of the three PCNA protomers through four contact points involving the AAA+ domains of Ctf18, RFC2, RFC4, and RFC5 (Fig 1c and Fig 3c). The interactions of PCNA with the RFC2 and RFC5 subunits are analogous to those reported in the hRFC–PCNA complex (10). However, while Ctf18 engages PCNA-I via a PIP-box interaction similar to hRFC1 (10), its atypical PIP motif — lacking aromatic residues (Fig. 2a and Fig. 3c) — results in a smaller buried surface area (~780 Å$^2$ vs. ~1010 Å$^2$). A methionine residue (M419) inserts into the so-called “Q-pocket,” which is typically occupied by a glutamine in canonical PIP-boxes, while V422 occupies the conserved hydrophobic pocket that usually accommodates aromatic residues. This low-affinity interaction does not stably anchor Ctf18 to PCNA-I and may contribute to the relative flexibility of the AAA+ domain of Ctf18 observed in the complex (Fig S2 and Supplementary Video 1). The PIP-box of RFC5 is also atypical but contains two hydrophobic residues (I114 and F115) that insert into the conserved pocket of PCNA-II. The interacting motifs of RFC2 and RFC4 differ from each other in sequence but both

engage similar regions involving the interdomain connecting loop (IDCL) of PCNA-I and PCNA-II, respectively (Fig 3d).

Interestingly, while RFC4 interacts with PCNA in the CTF18-RFC complex, it does not in the hRFC–PCNA complex (10). The RFC4–PCNA interaction, which was also observed in the structure of *S. cerevisiae* RFC bound to open PCNA (11), brings PCNA closer to the CTF18-RFC module, thereby explaining the distinct tilt of the PCNA ring observed in our structure compared to the hRFC–PCNA complex (Fig. 1c and 1d). Given the structure of scRFC bound to open PCNA (11), where all five RFC subunits are bound to PCNA (Fig 3d), we predict that a conformational shift in CTF18–RFC, specifically bringing the fifth subunit (RFC3) to engage PCNA-III, would be necessary to disrupt the interface between PCNA-I and PCNA-III, thereby opening the clamp and aligning the CTF18-RFC subunits for primer-template DNA interaction. The reason for the absence of such an active CTF18-RFC conformation in our cryo-EM analysis remains uncertain. However, similar to observations with the hRFC–PCNA complex, where an open-clamp state was not reported (10), this could be attributed to the hydrophobic regions of the open clamp interacting with the water-air interface, potentially leading to protein denaturation during the vitrification process to prepare the cryo-EM grids.

## Nucleotide binding to the AAA+ modules

The map is consistent with nucleotides in four of the five AAA+ domains of the CTF18-RFC subunits (Fig 4a). ATP is bound to subunits Ctf18, RFC2, and RFC5, while ADP appears to engage RFC3, consistent with the structure of the hRFC–PCNA complex

reconstituted with the slowly hydrolysable nucleotide ATPγS (10). Density for the adenine ring of ATP in the Ctf18 subunit is poor, likely a consequence of the increased mobility of the AAA+ domain of this subunit (Fig 4a). Compared to the canonical RFC1, the Walker A motif of Ctf18 contains a leucine residue (L378) instead of a valine, but this substitution does not appear to affect its interaction with the ATP nucleotide (Fig S5). Since RFC3 lacks critical catalytic residues and bears a substitution in the Walker A motif (10), the presence of ADP, rather than a product of ATP hydrolysis, probably results from co-purification of the complex where ADP contaminants are present. In the human RFC complex, it has been previously shown that an intact nucleotide binding site in RFC3 has an important structural role in the complex assembly (46, 47). If this is the case for CTF18-RFC, it remains to be established, but it is likely that ADP binding to this subunit may play a stabilizing role in all RFC-like loaders.

Differently from the hRFC–PCNA complex, where RFC4 is bound to ATPγS, in CTF18-RFC, this subunit is not engaged with a nucleotide (Fig 4a). The residues in the AAA+ of RFC4 of CTF18-RFC coordinated to ATPγS in hRFC are displaced and incompatible with nucleotide binding (Fig 4c). In particular, the side chains of R45 and P46 in RFC4 occupy the space where ATP would normally bind, thereby sterically hindering nucleotide accommodation in the CTF18-RFC structure (Fig 4c). Interestingly, mutation of the conserved K84 residue in the ATP-binding motif of RFC4 in hRFC did not impair the ability of this subunit to assemble with other RFC subunits (46, 47). In agreement, our structure shows that the lack of ATP binding to RFC4 does not preclude the assembly of the CTF18-RFC pentamer in the autoinhibited conformation. However, considering the importance of ATP binding of RFC4 for the hRFC clamp loading function

(48-51), it is expected that ATP binding to RFC4 in CTF18-RFC is required to switch to an enzymatically active conformation.

The asymmetric spiral of the CTF18-RFC AAA+ pentamer (Fig 4a-b) disrupts the active sites at the Ctf18/RFC2, RFC2/5, and RFC5/4 interfaces (Fig 4c). At these interfaces, the *trans*-acting arginine fingers are positioned too far away to interact with the γ-phosphate of ATP (*e.g.*, ~9 Å for R184 of RFC2, ~10 Å for R168 of RFC5, and ~7 Å for R193 of RFC4) (Fig 4c). Prior research has indicated that hydrolysis at the large subunit/RFC2 interface is not essential for clamp loading by various loaders (48-51), while the others are critical for the clamp-loading activity of eukaryotic RFCs.

In CTF18-RFC, the AAA+ spiral is overtwisted in a manner reminiscent of the autoinhibited conformations observed in hRFC and scRFC (8) (10) (Fig 1d), leading to steric hindrance that impedes DNA binding (Fig 4b). Specifically, the overtwisted RFC3 and RFC4 subunits occupy the space normally filled by DNA. In the autoinhibited structure of hRFC, the β-hairpin (residues 68-88) located at the base of RFC3 also referred to as "E-plug", extends towards the anticipated location of DNA and interacts with the Rossmann fold of RFC1 (10). Conversely, in CTF18-RFC, while this same β-hairpin is oriented toward the interior of the DNA-binding channel (Fig 4d), it does not make direct contact with the Ctf18 subunit. Collectively, the E-plug appears a conserved feature in eukaryotic clamp loaders, underlying its importance in maintaining the pentamer in its autoinhibited conformation, by preventing DNA access through the central channel. We observed that human CTF18-RFC shares an additional structural feature with both human and yeast RFC: the presence of a separation pin in the large subunit (10, 11). Although the separation pin is not essential for clamp loading (11), its

conservation across species and clamp loader types suggests an auxiliary or context-dependent function. Interestingly, residues W638 and F582—proposed to stabilize the separation pin and its interaction with DNA in yeast RFC—are substituted by F692 and H645 in human CTF18-RFC, respectively (Fig 4e), possibly indicating a mechanistically similar role in both systems.

To discount the possibility that the absence of the $Mg^{2+}$ ions in the cryo-EM sample could have hindered the proper assembly of the CTF18-RFCpentamer for DNA engagement, we used cryo-EM to visualize CTF18-RFC with PCNA, primer-template DNA, ATP, and $Mg^{2+}$ (Fig S6-7, S1 Table). Despite the inclusion of $Mg^{2+}$, the resulting 3.2 Å reconstruction of the complex remained in a configuration analogous to that without $Mg^{2+}$ (Fig 5a-b, Fig S6). In this reconstruction, distinct density for $Mg^{2+}$ is noted in the active sites of RFC2 and RFC5, coordinating ATP (Fig 5b). Similar to the map without $Mg^{2+}$, ADP coordination is present in RFC3, while RFC4 is not engaged with any nucleotide. These findings collectively imply that the presence of $Mg^{2+}$ in the nucleotide binding sites does not influence the transition of CTF18-RFC from an autoinhibited to an active state. This result also confirms the remarkable stability of the autoinhibited conformation, even in hydrolysing conditions.

## The Ctf18 β-hairpin plays a role in PCNA loading and in stimulating DNA synthesis by Pol ε

Based on the structures reported herein, the β-hairpin at the disordered N-terminal domain of Ctf18 is a distinctive feature that may serve to stabilize the CTF18-RFC pentamer and maximize its clamp loading efficiency. To investigate the functional

importance of the β-hairpin, we purified a CTF18-RFC mutant with a truncation at the disordered N-terminal domain of the Ctf18 subunit, specifically, the segment spanning residues 165-194 (CTF18$^{\Delta 165\text{-}194}$-RFC). This mutation eliminates the entire Ctf18 β-hairpin and is expected to destabilize the CTF18-RFC pentamer. In agreement, when mutant CTF18-RFC was imaged by cryo-EM with PCNA in the same conditions used for wild type CTF18-RFC, only a small subset of particles of the complex was observed, while the majority of particles contained dissociated PCNA (Fig S8-9). We hypothesized that this destabilizing mutation in CTF18-RFC may reduce its efficiency in loading PCNA onto DNA.

We directly compared clamp loading by CTF18-RFC, CTF18$^{\Delta 165–194}$-RFC and the canonical RFC complex, using a pre–steady-state ensemble FRET assay to monitor the loading of Cy5-labeled PCNA onto a Cy3-labeled primer–template DNA substrate pre-coated with RPA (Fig 6a, Figs S10-14). Prior to the addition of clamp loaders (Fig S11a), donor ($I_{563}$) and acceptor ($I_{665}$) fluorescence intensities remained low and stable over time (Fig S11b–d). Here, $I_{563}$ and $I_{665}$ correspond to the fluorescence intensities of the Cy3 donor (563 nm) and Cy5 acceptor (665 nm), respectively, and were used to calculate the apparent FRET efficiency ($E_{FRET}$). The constant $E_{FRET}$ values recorded during the first 60 s represent the experimental baseline ($Y_{Min}$) corresponding to the absence of interactions between Cy5–PCNA and the 5′ddPCy3/T·RPA nucleoprotein complex (52, 53). Upon addition of a clamp loader, $I_{665}$ increased concomitantly with a decrease in $I_{563}$, after which both signals stabilized, indicating the onset and persistence of FRET (Fig S11b–d). These synchronized, anti-correlated changes in donor and acceptor intensities report the loading of Cy5–PCNA onto the DNA substrate. After

reaching a plateau, $E_{FRET}$ values remained constant for at least 60 s, representing the amount of loaded and stably bound PCNA rings (52). For each condition, $E_{FRET}$ values within the final plateau region were fit to flat lines to determine the maximum $E_{FRET}$ ($Y_{Max}$) reached after clamp loader addition. Importantly, CTF18-RFC and CTF18$^{\Delta 165–194}$-RFC displayed similar dynamic ranges of $E_{FRET}$ values (i.e., $Y_{Max} – Y_{Min}$, Fig S11c-d), indicating that the β-hairpin deletion does not affect the overall extent of PCNA loading. All $E_{FRET}$ values measured after addition of each clamp loader were normalized to their respective dynamic ranges, defined by the baseline ($Y_{Min}$) and maximum ($Y_{Max}$) $E_{FRET}$ values, and plotted as a function of time following complex addition.

Under our experimental conditions, the clamp loader complexes must bind ATP and free PCNA before initiating loading, which can give rise to multiple kinetic phases. Such multiphasic behaviour has been described previously for RFC in stopped-flow experiments and is also evident in our ensemble FRET setup (52-54). The kinetic steps represented by each phase have been well defined for RFC but not for CTF18-RFC. In our measurements, the instrumental dead time was <7 s. Within this interval, a substantial fraction of PCNA loading (ranging from ~30% for CTF18-RFC to ~70% for RFC; Fig 6b-d) occurs, indicating clear kinetic differences among the clamp loader complexes but precluding full resolution of all reaction phases for CTF18-RFC.

To enable direct comparison of loading rates, only normalized $E_{FRET}$ values recorded after the dead time were fitted to the minimal kinetic model that yielded randomly distributed residuals. For CTF18-RFC, the data were best described by a single-exponential rise (Fig S12), whereas RFC and CTF18$^{\Delta 165–194}$-RFC required a double-exponential fit (Fig S13a–b), consistent with the presence of an additional kinetic

phase (Fig S13c–d). From these minimal models, we calculated the times required to reach 50%, 90%, and 95% of the maximal normalized $E_{FRET}$ signal ($t_{0.50}$, $t_{0.90}$, $t_{0.95}$), corresponding respectively to half completion and near completion of PCNA loading (Fig 6b-d and Fig S14). For RFC, $t_{0.50}$ occurred within the dead time and is thus reported as a lower limit (Fig 6b).

Across the three complexes, the kinetics of PCNA loading differed significantly (Fig 6b-d). RFC reached half completion within the experimental dead time ($t_{0.50} \leq 7$ s), consistent with rapid loading, whereas CTF18-RFC and CTF18$^{\Delta 165–194}$-RFC exhibited slower half-times of approximately 8 s and 12 s, respectively. Completion times further underscored these differences: both RFC and CTF18-RFC reached 95 % completion at ~77 s, while the CTF18$^{\Delta 165–194}$-RFC mutant required ~145 s. This indicates that the β-hairpin deletion significantly slows the reaction progression. Altogether, the results from these FRET studies (Fig 6, Fig S10–S14) indicate that deletion of the β-hairpin from CTF18 does not affect the overall extent of PCNA loading but rather slows the reaction progression.

We then tested whether the observed loading defect observed with CTF18$^{\Delta 165\text{-}194}$-RFC results in diminished stimulation of primer synthesis by Pol ε. To test this hypothesis, we performed primer extension assays using Pol ε, PCNA, and either wild-type or mutant CTF18-RFC constructs to assess their ability to stimulate DNA synthesis by Pol ε. Our results indicate a significant reduction in primer extension products when the β-hairpin was deleted (Fig 7a). Measurement of band intensities revealed an approximately two-fold decrease in the amount of extended primer produced by the mutant compared to the wild-type (Fig 7b). To further support that the observed effect on

primer extension is due to the mutation, we conducted a concentration titration comparing wild-type and mutant CTF18-RFC (Fig S15). The CTF18-RFC mutant displayed altered concentration dependencies compared to the wild-type, thereby validating the mutant phenotype and underscoring the structural importance of the β-hairpin feature. Notably, the primer extension assay was conducted with 2 nM plasmid DNA and excess CTF18-RFC (40 nM), PCNA (100 nM), and Pol ε (30 nM), establishing single-turnover conditions per DNA molecule. Under these conditions, the rate—not the extent—of PCNA loading becomes the key determinant of synthesis dynamics. Although Pol ε can initiate synthesis independently of PCNA, the clamp is required for full processivity. Therefore, the slower loading rate observed for the CTF18-RFC mutant likely delays formation of highly processive complexes, resulting in a slower accumulation of extended products and explaining the observed ~2-fold reduction in synthesis.

# Discussion

In this work, we reported the structure of the human CTF18-RFC clamp loader bound to PCNA in the presence of ATP with or without $Mg^{2+}$ ions. Our cryo-EM data, together with previous work (34) (37), support that the Ctf8 and Dcc1 subunits of CTF18-RFC, forming the regulatory module interacting with Pol ε (37), are flexibly tethered to the RFC-module via binding to the Ctf18 C-terminus, which is separated by the N-terminal RFC1-like module of Ctf18 by ~90 amino acid flexible linker. Therefore, CTF18-RFCcomprises two structurally distinct modules that cooperate to load PCNA onto the leading strand, facilitating replication by Pol ε.

The CTF18-RFC–PCNA complex was observed in an autoinhibited conformation, which prevents DNA binding. This mirrors the similar conformation in hRFC and scRFC, as previously reported (10), (11). Such conformation represents a transient encounter complex that occurs early in the clamp loading process, before the opening of the clamp. Despite the variations in the large RFC subunit in the two assemblies, we demonstrate a striking architectural conservation between the alternative human clamp loader CTF18-RFCand the canonical RFC. Specifically, CTF18-RFC utilizes four subunits (Ctf18, RFC2, RFC5, and RFC4) to engage two PCNA protomers. However, the engagement of the third PCNA protomer by RFC3 is necessary to initiate the opening of the PCNA ring interface, a process that requires a conformational shift of the AAA+ pentamer from an autoinhibited to an active state. Supporting this, previous structural studies on scRFC have shown that the conformation of RFC bound to open PCNA is facilitated through a 'crab-claw' mechanism, which is inherently predisposed to DNA binding (11). This conformational change creates an opening between the A′ segment and the AAA+ module in the A subunit, allowing primer-template DNA to bind within the RFC inner chamber (11) (Fig 4C). Remarkably, this significant conformational shift occurs rapidly (55), does not depend on ATP hydrolysis, and ensures the sequential binding of PCNA and the DNA substrate in the correct order. While our study did not resolve the active conformation of CTF18-RFC, the observed structural conservation in the autoinhibited state, particularly of the large Ctf18 subunit (Fig 2), suggests that a similar 'crab-claw' mechanism may facilitate the transition of CTF18-RFC to its active state for PCNA opening and DNA binding. While our work was being finalized, several cryo-EM structures of human CTF18-RFC bound to PCNA, and

primer/template DNA were reported by another group (56). These findings are consistent with the distinct features of CTF18-RFC observed in our structures and independently support the notion of significant mechanistic similarity between CTF18-RFC and canonical RFC in loading PCNA onto a ss/dsDNA junction.

The main structural differences between CTF18-RFC and the canonical RFC include increased mobility of the large subunit and the presence of a β-hairpin that attaches to the RFC5 subunit. The mobility of the large subunit is likely enhanced by the low-affinity PIP motif that anchors it to the PCNA ring. We propose that the β-hairpin may have evolved to counterbalance the mobility of the large subunit, helping to maintain its connection to the RFC pentamer and stabilizing the clamp loader structure. Collectively, our structural and biochemical analyses reveal that removal of the β-hairpin compromises the stability of the CTF18-RFC–PCNA complex, results in slower clamp loading kinetics, and leads to reduced stimulation of Pol ε primer synthesis, consistent with a defect in the rate of PCNA loading (Fig 8). Interestingly, a recent work reporting cryo-EM structures of the yeast homolog of CTF18-RFC bound to PCNA (56) does not support the presence of a stable β-hairpin at the N-terminus of the Ctf18 subunit engaged to the collar of the Rfc3 subunit. Therefore, the functional β-hairpin we observed in human CTF18-RFC appears a distinct feature that pertains to higher eukaryotes, required to maximize the activity of CTF18-RFC in loading PCNA onto the leading strand.

# Materials and Methods

## Protein expression and purification

## Preparation of CTF18-RFC

MultiBac™ expression system (Geneva Biotech) was used to express human Ctf18-RFC2-5 along with two additional cohesion-specific factors, Dcc1 and Ctf8 (named hereafter CTF18-RFC) in Sf9 insect cells. For this purpose, insect cells optimized sequences of N-terminus twin Strept-tagged TEV Ctf18, RFC2, and RFC4 were cloned in pACEBac1 plasmid with independent promoters and terminators, and N-terminus 6X histidine-tagged RFC3, RFC5, Dcc1 and Ctf8 were cloned in pIDS plasmid with independent promoters and terminators by GenScript. Finally, the single transfer vector with different subunit assemblies was generated using *cre* recombinase according to the MultiBac™ expression system user manual. CTF18-RFC encoding all seven subunits in a single MultiBac™ expression plasmid (pACEBac1) was transformed into DH10MultiBac™ cells to make bacmid DNA. To prepare the baculovirus, bacmid DNA containing all subunits was transfected into Sf9 cells using FuGENE® HD (Promega) according to the manufacturer's instructions. This baculovirus prep was amplified twice to obtain a higher titer virus (P3 virus). The expression of CTF18-RFC then proceeded by transfecting a 6 L Hi5 suspension culture at a density of $2 \times 10^6$ cells/mL with the P3 virus for 60-65 hours.

Cells were collected by centrifugation at 5,500 xg for 10 minutes and re-suspended in lysis buffer [50 mM Tris-HCl (pH 7.5), 300 mM NaCl, 20 mM imidazole, 5 mM BME, 0.1% Nonidet P-40, 10% glycerol and one EDTA-free protease inhibitor cocktail tablet/50 mL]. All further steps were performed at $4^{o}$ C. Cells were sonicated and debris was removed by centrifugation at 95,834 xg for 1 hour at 4 °C. The resultant supernatant was directly loaded onto a HisTrap HP 5 mL affinity column (Cytiva) pre-

equilibrated with buffer A [50 mM Tris-HCl (pH 7.5), 300 mM NaCl, 20 mM imidazole, 5 mM BME and 10% glycerol]. After loading, the column was washed with 50 mL of buffer A and the bound fractions were eluted by gradient with 50 mL of buffer B [50 mM Tris-HCl (pH 7.5), 300 mM NaCl, 500 mM imidazole, 5 mM BME, and 10% glycerol]. The eluents were pooled and directly loaded onto Strept Trap XT 1 mL affinity column pre-equilibrated with buffer A [50 mM Tris-HCl (pH 7.5), 300 mM NaCl, 5 mM BME and 10% glycerol]. After loading, the column was washed with 10 mL of buffer A, followed by step elution with buffer B [50 mM Tris-HCl (pH 7.5), 300 mM NaCl, 50 mM Biotin, 5 mM BME, and 10% glycerol]. Eluents were pooled and incubated with the TEV protease overnight. Fractions were concentrated to 1 mL and loaded onto HiLoad 16/600 Superdex 200 pg pre-equilibrated with gel filtration buffer [50 mM Tris-HCl (pH 7.5), 200 mM NaCl, 1 mM DTT, and 10% glycerol]. Protein fractions were pooled in a total volume of 1.6 mL, flash frozen, and stored at -80°C.

## Preparation of PCNA

To express PCNA BL21(DE3) *E. coli* cells were transformed with WT PCNA plasmid. The transformed cells were grown at 37°C in 2YT media supplemented with ampicillin to an OD600 of 1.2. The cell cultures were induced with 0.5 mM isopropyl-beta-D-1-thiogalactopyranoside (IPTG) and let them grow for 19 hours at 16°C. Cells were then harvested by centrifugation at 5500 xg for 10 minutes and then re-suspended in lysis buffer [50 mM Tris-HCl (pH 7.5), 750 mM NaCl, 20 mM imidazole, 5 mM BME, 0.2% Nonidet P-40, 1 mM PMSF, 5% glycerol and one EDTA-free protease inhibitor cocktail tablet/50 mL]. The cells were lysed with 2 mg/mL of lysozyme at 4°C for 30 minutes.

Cells were sonicated and debris was removed by centrifugation at 22,040 xg for 20 minutes at 4°C. The cleared cell lysate was directly loaded onto a HisTrap HP 5 mL affinity column (Cytiva) pre-equilibrated with buffer A [50 mM Tris-HCl (pH 7.5), 500 mM NaCl, 20 mM imidazole, 5 mM BME and 5% glycerol]. The column was firstly washed with 50 mL of buffer A and then with 50 mL of buffer B containing low salt [50 mM Tris-HCl (pH 7.5), 100 mM NaCl, 500 mM imidazole, 5 mM BME, and 5% glycerol]. The eluents were pooled and directly loaded onto HiTrap Q HP 5 mL anion exchange column (GE Healthcare) pre-equilibrated with buffer D [50 mM Tris-HCl (pH 7.5), 100 mM NaCl, 5 mM BME and 5% glycerol]. The column was washed with 50 mL of buffer D after loading, followed by elution of 50 mL gradient with buffer E [50 mM Tris-HCl (pH 7.5), 1 M NaCl, 5 mM BME, and 5% glycerol]. Eluents were pooled and concentrated to 1.5 mL and loaded onto HiLoad 16/600 Superdex 200 pg pre-equilibrated with gel filtration buffer [50 mM Tris-HCl (pH 7.5), 150 mM NaCl, 1 mM DTT, and 5% glycerol]. Protein fractions were pooled, flash-frozen, and stored at -80 °C. Human RPA, Cy5-PCNA, and RFC for the clamp loading assay were obtained as previously described (57) (58). The concentration of active RPA was determined via a FRET-based activity assay as described previously (59).

## Preparation of DNA polymerase ε

MultiBac™ expression system (Geneva Biotech) was used to express human DNA Pol ε in Sf9 insect cells. For this purpose, insect cells optimized sequence of the catalytic subunit, p261 was cloned in pACEBac1 and p59, C-terminus TEV twin Strept-tagged p17, and N-terminus 8X histidine-tagged TEV p12 along with independent promoters and terminators were cloned in pIDS by the GenScript. Finally, the single transfer vector

with different subunit assemblies was generated using *cre* recombinase according to MultiBac™ expression system user manual. To prepare the baculovirus, the bacmid DNA of Pol ε was transfected into Sf9 cells using FuGENE® HD (Promega) according to the manufacturer's instructions. The resulting supernatant was obtained as the P1 virus stock which was then amplified to obtain P2 virus stock. P2 virus stock was then further amplified to obtain P3 virus stock for large-scale expression. Pol ε was expressed by transfecting 4 L of Sf9 suspension culture at $2 \times 10^6$ cells/mL density with P3 virus. Cells were harvested after 72 hours by centrifugation at 5,500 xg for 10 minutes and re-suspended in 200 mL of lysis buffer [50 mM HEPES (pH 8), 20 mM Imidazole, 400 mM NaCl, 5 mM β-Mercaptoethanol, 5% (v/v) Glycerol, 0.1% NP-40, 1 mM PMSF and EDTA-free protease inhibitor cocktail tablet/50 mL (Roche, UK)]. Cells were sonicated and debris was removed by centrifugation at 95,834 xg for 1 hour at 4 °C. The resultant supernatant was directly loaded onto a HisTrap HP 5 mL affinity column (Cytiva) equilibrated with buffer A [50 mM HEPES (pH 8), 20 mM Imidazole, 400 mM NaCl, 5mM β-Mercaptoethanol, 5% (v/v) Glycerol and EDTA-free protease inhibitor cocktail tablet/50 mL (Roche, UK]. After loading, the column was washed with 50 mL of buffer A and the bound fractions were eluted by gradient with 50 mL of buffer B [50 mM HEPES (pH 8), 500 mM Imidazole, 300 mM NaCl, 5 mM β-Mercaptoethanol, 5% (v/v) Glycerol and EDTA-free protease inhibitor cocktail tablet/50 ml (Roche, UK)]. Peak fractions containing Pol ε subunits were pooled and loaded directly onto Strep Trap XT 5 mL (Cytiva) column equilibrated with buffer C [50 mM HEPES (pH 8), 250 mM NaCl, 5 mM β-Mercaptoethanol, 5% (v/v) Glycerol] and EDTA-free protease inhibitor cocktail tablet/50 mL (Roche, UK)]. After loading, the column was washed with 50 mL of buffer C

and the bound fractions were incubated for 2-4 hours with 15 mL of 100% buffer D [50 mM HEPES (pH 8), 100 mM NaCl, 50 mM Biotin, 5 mM β-Mercaptoethanol, 5% (v/v) Glycerol] and EDTA-free protease inhibitor cocktail tablet/50 mL (Roche, UK)] and eluted further with 30 mL of 100% buffer D. Fractions that contain all Pol ε subunits were pooled and incubated with the TEV protease for overnight and loaded onto an anion exchanger, Mono Q 5/50 GL column (Cytiva) pre-equilibrated with buffer E [50 mM HEPES (pH 8), 100 mM NaCl, 5 mM β-Mercaptoethanol and 5% Glycerol]. After loading, the column was washed with 15 mL of buffer E. The Pol ε was eluted with a 10 mL gradient from 100 mM NaCl to 1 M NaCl in 50 mM HEPES (pH 8), 5 mM β-Mercaptoethanol, and 5% Glycerol. The fractions that contained all Pol ε subunits were combined and concentrated to 1 mL and loaded onto HiLoad 16/600 Superdex 200 pg (Cytiva) pre-equilibrated with gel filtration buffer [50mM HEPES (8), 200 mM NaCl, 1 mM DTT and 5% Glycerol]. Protein fractions were pooled, flash-frozen, and stored at −80°C.

All protein concentrations were calculated by measuring their absorbance at 280 nm using the extinction coefficients calculated from the amino acid composition (CTF18-RFC: 216,360 $M^{-1}$ $cm^{-1}$; PCNA: 47,790 $M^{-1}$ $cm^{-1}$, Pol ε: 351,470 $M^{-1}$ $cm^{-1}$).

## DNA substrates for Cryo-EM

For the primer/template substrates used in all the structures described here, 80 base pairs template strand 5'-TTTTTTTTTTTTTTTTTTTTTTTTTTTTTTTTTTTTTTTTGACTGCAC

GAATTAAGCAATTCGTAATCATGG TCATAGCT-3' was annealed to a 39 base pairs primer containing a 3' dideoxy cytosine chain terminator 5'-AGCTATG ACCATGATTACGAATTGCTTAATTCGTGCAGT[ddC]-3' to form the P/T substrate. The strands were mixed in an equimolar ratio in the presence of 20 mM Tris pH 7.5 and 25 mM NaCl. The annealing reaction was performed by incubating the P/T at 92°C for 2 minutes followed by slow cooling to room temperature overnight. All oligonucleotides were purchased from IDT Integrated DNA Technologies.

## Clamp loading and primer extension substrates

Oligonucleotides for the clamp loading assay comprising the 5′ddPCy3/T P/T DNA substrate were synthesized by Integrated DNA Technologies (Coralville, IA) or Bio-Synthesis (Lewisville, TX) and purified on denaturing polyacrylamide gels. The concentrations of unlabeled DNAs were determined from the absorbance at 260 nm using the provided extinction coefficients. Concentrations of Cy3-labeled DNAs were determined from the extinction coefficient of Cy3 at 550 nm ($\varepsilon_{550}$ = 136,000 $M^{-1}cm^{-1}$). For annealing the 5′ddPCy3/T P/T DNA substrate (as depicted in Fig S10), the primer and corresponding complementary template strand were mixed in equimolar amounts in 1X annealing buffer (10 mM TrisHCl, pH 8.0, 100 mM NaCl, 1 mM EDTA), heated to 95 $^{o}$C for 5 minutes, and allowed to slowly cool to room temperature. For the prime extension assay, Oligo (592:TAACGCCAGGGTTTTCCCAGTCACG) (Integrated DNA Technologies) was annealed to 50 nM M13mp18 single-stranded DNA (New England Biolabs) in a reaction buffer consisting of [10 mM Tris-HCl (pH 7.6), 100 mM NaCl and 5 mM EDTA]. The mixture was heated to 95 °C for 5 minutes, then cooled gradually to

room temperature. The unannealed oligonucleotide was removed using a QIAquick PCR purification kit (Qiagen).

## Pre-steady state FRET measurements

All experiments were performed at room temperature (23 ± 2 °C) in a 16.100F-Q-10/Z15 sub-micro fluorometer cell (Starna Cells) and monitored in a Horiba Scientific Duetta-Bio fluorescence/absorbance spectrometer as described previously (52). In short, reaction solutions are excited at 514 nm and the fluorescence emission intensities (*I*) are monitored essentially simultaneously (Δt = 0.118 ms) at the peak emission wavelengths for Cy3 (563 nm, $I_{563}$) and Cy5 (665 nm, $I_{665}$) over time, recording *I* every 0.17 s. For all experiments, excitation and emission slit widths are 10 nm. All recorded fluorescence emission intensities are corrected by a respective dilution factor and all-time courses are adjusted for the time between the addition of each component and the fluorescence emission intensity recordings (i.e., dead time ≤ 7 s). For any recording of the fluorescence emission intensities ($I_{665}$ and $I_{563}$), the approximate FRET efficiency is estimated from the equation $E_{FRET} = \frac{I_{665}}{I_{665}+I_{563}}$. For each experiment below, the final concentrations of all reaction components are indicated.

PCNA loading experiments were carried out in 1X Replication Buffer (25 mM HEPES, pH 7.5, 125 mM KOAc, 10 mM $Mg(OAc)_2$) supplemented with 1 mM DTT, 1 mM ATP, and the ionic strength adjusted to physiological (200 mM) by addition of KOAc. Experiments were performed via slight modifications to a published protocol (52) (53). In short, 5′ddPCy3/T P/T DNA (200 nM, NeutrAvidin (800 nM homotetramer), and ATP (1 mM) are pre-incubated with RPA (600 nM heterotrimer). Then, Cy5-PCNA (200 nM

homotrimer) is added, the resultant solution is transferred to a fluorometer cell, and the cell is placed in the instrument. $I_{665}$ and $I_{563}$ are monitored until both stabilize for at least 1 min. Finally, a given clamp loader complex (200 nM RFC, CTF18-RFC, or CTF18$^{D165-194}$-RFC henteropentamer) is added, the resultant solution is mixed, and $I_{665}$ and $I_{563}$ are monitored, beginning $\leq$ 7 s after the addition of the respective clamp loader complex (i.e., "dead time" = Dt $\leq$ 7 s).

## Primer extension assay

The primer extension reaction was conducted in a reaction buffer containing [40 mM HEPES (pH 7.6), 100 mM K-glutamate, 1 mM DTT, 10 mM Mg-Acetate, 200 µg/mL BSA, 1 mM ATP, 100 µM each of dATP, dTTP, and dGTP, 20 µM dCTP, and 10 µCi of [$^{32}$P]-dCTP (Hartmann)]. Two nanomolar of the primed-M13 template were initially incubated at 37 °C for 10 minutes with 100 nM PCNA, 400 nM RPA, and either CTF18-RFCWT or CTF18$^{\Delta 165-194}$-RFC. The reaction was initiated by the addition of 30 nM Pol ε. Reactions were stopped at the indicated time point by adding 50 mM EDTA and electrophoresed on 0.7% alkaline agarose gel at 35 V for 17 hours. The gel was backed with DE81 paper, compressed, and imaged in a Sapphire Biomolecular Imager (Azure Biosystems). All the experiments were performed in triplicate.

## Cryo-EM grids preparation and data collection

For all the complexes (WT and mutant), UltraAuFoil® R1.2/1.3 Au 300 grids were glow-discharged at 30 mA for 30 seconds on an EasyGlow glow-discharge unit. For the preparation of the complex without $Mg^{2+}$ **(Dataset 1 and Dataset 3)**, P/T DNA, ATP, CTF18-RFC WT/CTF18$^{\Delta 165-194}$-RFC, and PCNA were mixed in order. The final concentrations were 5.6 μM P/T DNA, 0.2 mM ATP, 1.5 μM CTF18-RFC WT/CTF18$^{\Delta 165-194}$-RFC, and 7.5 μM PCNA. The buffer this was performed in comprised 50 mM Tris-HCl pH 7.5, 200 mM NaCl, 1 mM DTT, and 0.5 mM ATP. 3 μL of the sample was applied to the grid, blotted for 2 s at blot force -5, and plunged frozen into liquid ethane using a Vitrobot Mark IV (FEI Thermo Fisher), which was set at 4°C and 100% humidity. For the preparation of CTF18-RFC/PCNA/P-T DNA/ATP/$Mg^{2+}$complex **(Dataset 2)**, the components P/T DNA, ATP, $Mg^{2+}$, CTF18-RFC, and PCNA were mixed in order. The final concentrations were 5.6 μM P/T DNA, 0.2 mM ATP, 1.9 mg/mL $Mg^{2+}$, 1.5 μM CTF18-RFC, and 7.5 μM PCNA. The buffer this was performed in comprised 50 mM Tris-HCl pH 7.5, 200 mM NaCl, 1 mM DTT, 0.5 mM ATP, and 5 mM $Mg^{2+}$. 3 μL of the sample was applied to the grid in the same way as above for data collection. Cryo-EM data for all the samples were collected on a Thermo Fisher Scientific Titan Krios G4 transmission electron microscope at KAUST. Electron micrographs for **Dataset 1** (CTF18-RFC-PCNA with ATP in the absence of $Mg^{2+}$), were collected using a Falcon 4i detector at a dose rate of 7.5 $e^-$/pix/sec for 5 seconds and a calibrated pixel size of 0.93 Å. Focusing was performed over a range between -2.7 μm and -1.5μm, in 0.3 μm intervals. Electron micrographs for **Dataset 2** (CTF18-RFC-PCNA with ATP and $Mg^{2+}$) were collected using a Falcon 4i detector at a dose rate of 8.02 $e^-$/pix/sec for 5 seconds and a calibrated pixel size of 0.93 Å. Focusing was performed over a range between -

2.7 µm and -1.5 µm, in 0.3 µm intervals. Electron micrographs for **Dataset 3** (CTF18$^{\Delta 165-194}$-RFC-PCNA with ATP and in the absence of $Mg^{2+}$) were collected using a Falcon 4i detector at a dose rate of 7.4 $e^-$/pix/sec for 5 seconds and a calibrated pixel size of 0.93 Å. Focusing was performed over a range between -2.7 µm and -1.5 µm, in 0.3 µm intervals.

## Cryo-EM image processing

Preprocessing of all datasets (**Dataset 1**: CTF18-RFC, ATP, primer/template DNA and PCNA; **Dataset 2:** CTF18-RFC, ATP, $Mg^{2+}$, primer/template DNA and PCNA; **Dataset 3**: CTF18$^{\Delta 165-194}$-RFC, ATP, primer/template DNA and PCNA) was performed as follows: the micrographs were corrected for beam-induced motion and then integrated using MotionCor2 (60). All frames were retained and a patch alignment of 4x4 was used. CTFFIND-4.12 estimated Contrast Transfer Function (CTF) parameters for each micrograph (61). Integrated movies were inspected with Relion-4.0 (**Dataset 1** and **Dataset 2**) and Relion-5.0 (**Dataset 3**) for further image processing (7906 movies for **Dataset 1**, 6181 movies for **Dataset 2**, and 6499 movies for **Dataset 3**) (62). Particle picking was performed in automated mode using Topaz (63) for **Dataset 1**. Particle extraction was carried out from micrographs using a box size of 55 pixels (pixel size: 3.65 Å/pixel). An initial dataset of 2 x $10^6$ particles was cleaned by 2D classification followed by 3D classification with alignment. Three 3D classes were generated with populations of 31, 28, and 40%. 3D refinement, CtfRefine, and polishing were performed on the selected 3D classes corresponding to populations 31 and 40%. A

bigger box size, 480 pixels (pixel size: 0.93 Å/pixel) was used to re-extract the particles. 3D refinement, CtfRefine, and polishing yielded reconstruction at 2.9 Å.

Particle picking was performed in reference-based mode for **Dataset 2**. Particle extraction was carried out from micrographs using a box size of 55 pixels (pixel size of 3.65 Å/pixel). An initial dataset of 3 x $10^6$ particles was cleaned by 2D classification followed by 3D classification with alignment. Three 3D classes were generated with 30, 33, and 36% populations. 3D refinement, CtfRefine, and polishing were performed on the selected 3D classes corresponding to populations 33 and 36%. 3D refinement, CtfRefine, and polishing yielded reconstruction at 3.2 Å. Particle picking was performed in automated mode using Topaz (63) for **Dataset 3**. Particle extraction was done from micrographs using a box size of 220 pixels (pixel size: 0.93 Å/pixel). An initial dataset of 1 x $10^6$ particles was cleaned by 2D classification. For quantification of complex stability, the number of particles contributing to each 2D class was extracted from the classification metadata (**Datasets 1** and **3**). All classes showing isolated PCNA rings were summed and compared to the total number of particles in classes representing intact CTF18-RFC–PCNA complexes. This analysis was performed for both wild-type and β-hairpin deletion mutant datasets. Notably, no 2D classes corresponding to free PCNA were observed in the wild-type dataset, whereas in the mutant dataset, a substantial fraction of particles corresponded to isolated PCNA, suggesting reduced stability of the mutant complex.

## Cryo-EM 3D Variability Analysis

3DVA (43) (44) of the CTF18-RFC–PCNA consensus maps, with and without $Mg^{2+}$, was performed in CryoSPARC v 4.6 using their respective refinement masks, employing three modes and a resolution filter of 5 Å, based on global FSC resolutions of 2.9 Å and 3.2 Å, respectively. For each mode, 3 frames were generated and morphed to visualize the conformational flexibility across the components.

## Molecular Modelling

The structure of the Ctf18 large subunit of human CTF18-RFC (Q8WVB6, residues 277-805) was generated with Phyre2 (64), using as a template the sequence of human RFC1 (P35251, residues 581-1034). The Ctf18 subunit model was then aligned to the RFC1 subunit in the structure of the human RFC clamp loader bound to PCNA in an autoinhibited conformation (PDB 6VVO, (10)) using Chimera, the RFC1 subunit was deleted, and the resulting model including Ctf18, subunits RFC2-5 and PCNA was rigid-body fitted into the cryo-EM map. The model was edited and real-space refined with Coot (65) following flexible fitting performed with ISOLDE (66). A final real-space refinement was performed in Phenix (67), applying secondary structure constraints. The models of both CTF18-RFC–PCNA complexes with and without the $Mg^{2+}$ ion were generated similarly.

# Acknowledgments

This research was supported by King Abdullah University of Science and Technology (KAUST) through core funding (to S.M.H. and A.D.B.). We thank Lingyun Zhao, Ashraf Al-Alamoudi, Alessandro Genovese and Rachid Sougrat for their assistance at the

Imaging and Characterization Core Lab at KAUST. This work was also supported by funding from the National Institutes of Health to M.H. (R35 GM147238-03). This publication was supported, in part, by NIH Grant T32GM149417.

# Author Contributions

S.M.H. and A.D.B. conceived and supervised the study. M.T. and A.A. prepared proteins, carried out primer extension assays and analyzed the data. G.Y. and M.H. prepared proteins, carried out clamp loading assays and analyzed the data. G.R.B. and C.G.S. performed cryo-EM imaging and processing. A.U.D. performed the cryo-EM 3DVA analysis. G.R.B., P.Q-N., and A.D.B. performed model building and validation. A.D.B. wrote the manuscript with contributions from the other authors.

# Data Availability

The maps of CTF18-RFC-ATP-PCNA and CTF18-RFC-ATP-$Mg^{2+}$-PCNA complexes have been deposited in the EMBD with accession codes EMD-60534, and EMD-60598 and the atomic models in the Protein Data Bank under accession codes PDB 8ZWO and PDB 9IIN.

# Ethics declarations

*Competing interests*

The authors declare no competing interests.

# Figures

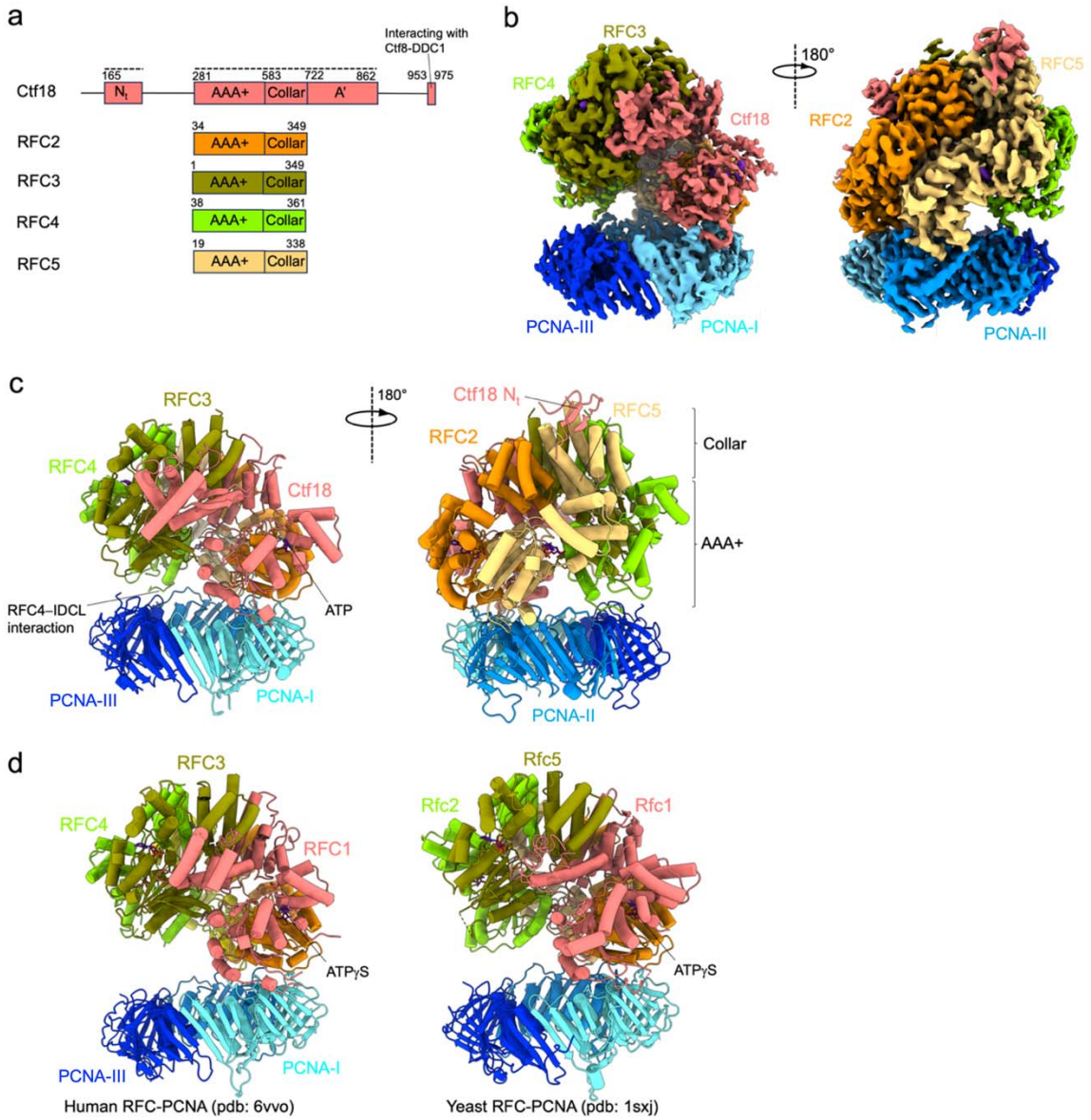


**Figure 1**. ***Cryo-EM structure of the human CTF18-RFC–PCNA complex in the presence of ATP.*** **a)** Domain organization of the CTF18-RFC subunits forming the RFC pentamer. The dotted line above the Ctf18 subunit highlights the regions that are observed in the cryo-EM map. **b)** Two views of the cryo-EM map of the CTF18-RFC–PCNA complex, coloured by subunits. The less sharp definition of the map region corresponding to the AAA+ domain of the Ctf18 subunit supports a relative high mobility

of this subunit. **c)** Molecular model of the CTF18-RFC–PCNA complex in ribbon representation. **d)** Structures of the human (left) and *Saccharomyces cerevisiae* (right) RFC–PCNA complex, which present the RFC pentamer in an auto-inhibited conformation analogous to the one captured in the CTF18-RFC–PCNA complex.

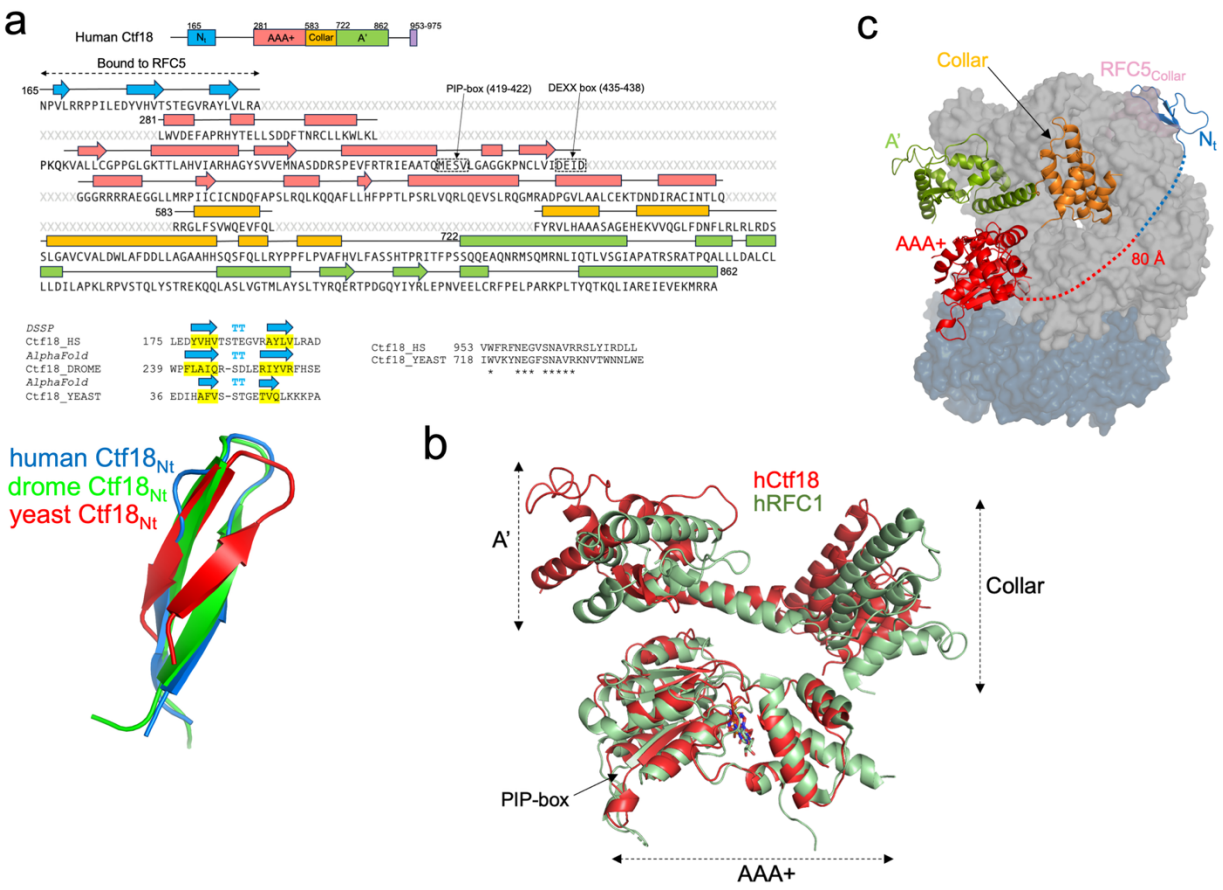

**Figure 2**. ***Structure of the Ctf18 subunit.*** **a)** Sequence of the human Ctf18 subunit, highlighting the secondary structural elements as assigned in the cryo-EM model. The atypical PCNA-interacting motif (PIP-box) and conserved DEXX box are boxed. Residues that are not modelled in the cryo-EM structure are labelled as X in grey. Below the Ctf18 sequence to the left, the sequences of the N-terminus of human and other lower eukaryotes Ctf18, together with the secondary prediction by AlphaFold (45) are shown, highlighting the conservation of the β-hairpin fold. Below, the cryo-EM β-hairpin fold model is overlaid onto the corresponding motifs predicted by AlphaFold for *Drosophila* or *Saccharomyces cerevisiae* Ctf18. Below the Ctf18 sequence to the right, the alignment of the C-terminal region of human and *Saccharomyces cerevisiae* Ctf18, which interacts with the Ctf8/Dcc1 subunits, is shown. Asterisks denote conserved residues. **b)** Superposition of the human Ctf18 and RFC1 (PDB: 6VVO) subunit structures, with subdomains labelled. **c)** Structure of the Ctf18 subunit, in ribbon representation, within the CTF18-RFC–PCNA complex. The Ctf18 subdomains are coloured-coded as in panel **(a)**. The other complex subunits are shown as surfaces.

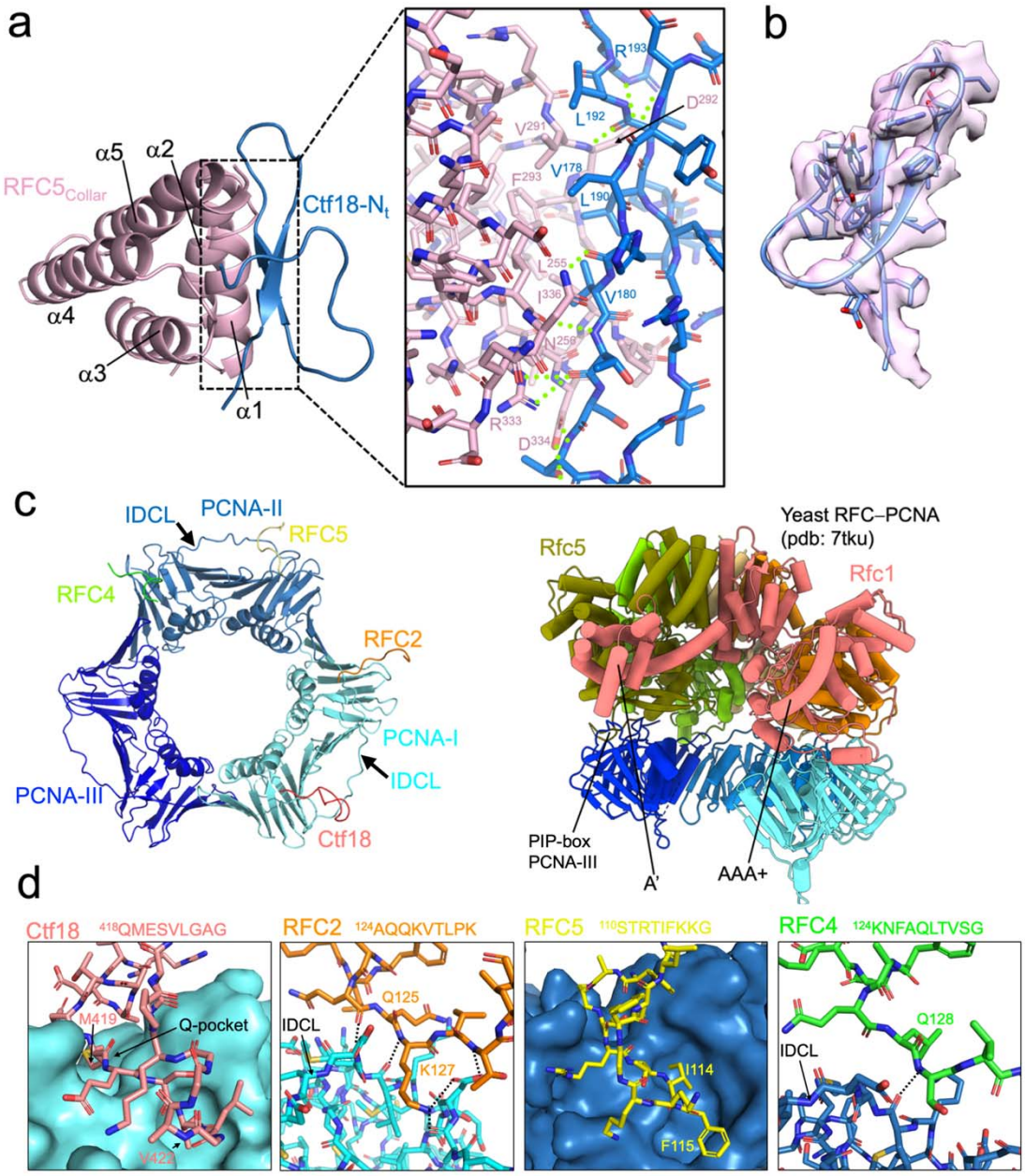


**Figure 3**. ***Structural details of the Ctf18–RFC5 and CTF18-RFC–PCNA interactions.*** **a)** Model of the RFC5 collar domain and Ctf18 N-terminal β-hairpin in ribbon representation. The inset shows the interface in stick representation, with hydrogen bonds shown as green dotted lines. **b)** Map region around the Ctf18 N-terminal β-

hairpin. **c)** Model of the PCNA homotrimer bound to the four CTF18 interacting regions. To the right, the structure of the yeast RFC–PCNA complex with an open clamp, highlighting the engagement of all five RFC subunits to PCNA, required for clamp opening. **d)** Model of the regions of the CTF18-RFC–PCNA interactions, with CTF18-RFC subunit residues shown as sticks and PCNA as surface or ribbon. Polar interactions are shown as black dotted lines. The amino acid sequence encompassing the interacting motifs in the various subunits are shown.

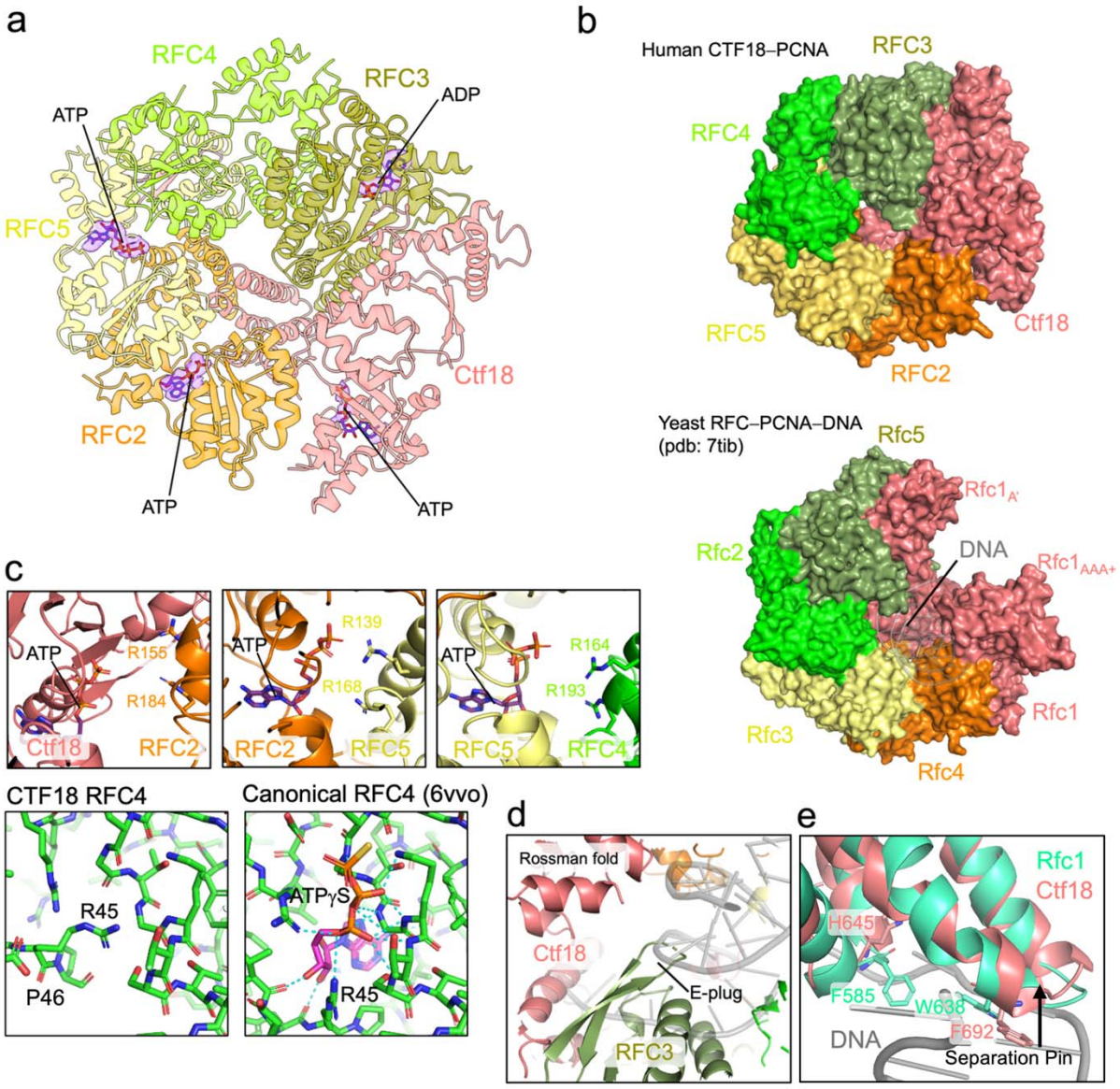


**Figure 4**. ***Analysis of the auto-inhibited conformation of the CTF18 pentamer and nucleotide coordination*. a)** Ribbon model of the CTF18-RFC pentamer (PCNA hidden). Nucleotide molecules are shown as sticks, with the corresponding cryo-EM density. **b)** Surface representation of (top) the CTF18-RFC pentamer and (bottom) the yeast RFC pentamer bound to open PCNA and primer-template DNA. PCNA is hidden in both structures. The overtwisted CTF18-RFC pentamer cannot accommodate DNA

within the inner chamber. **c)** Model of the ATP active sites in the CTF18-RFC–PCNA complex, showing disruption of the interactions mediated by the arginine fingers. Below, insets show the nucleotide-binding site of subunit RFC4 in either the human CTF18-RFC (left) or human RFC (right) models, highlighting the structural incompatibility with nucleotide binding in the CTF18-RFC structure. Polar interactions with ATPγS in human RFC4 are indicated as cyan dotted lines. **d)** Detail of the inner chamber region of the CTF18-RFC pentamer, showing the β-hairpin (E-plug) of RFC5 protruding in the region predicted to be occupied by DNA. The DNA (grey ribbon) is modeled as in the yeast RFC–DNA–PCNA complex. **e)** The structures of the RFC1 subunit from the yeast RFC–DNA–PCNA complex (11) and the Ctf18 subunit from the CTF18-RFC–PCNA complex are aligned to highlight conservation of the separation pin. Side chains of residues implicated in this motif in yeast RFC, along with the corresponding amino acids in CTF18-RFC, are shown.

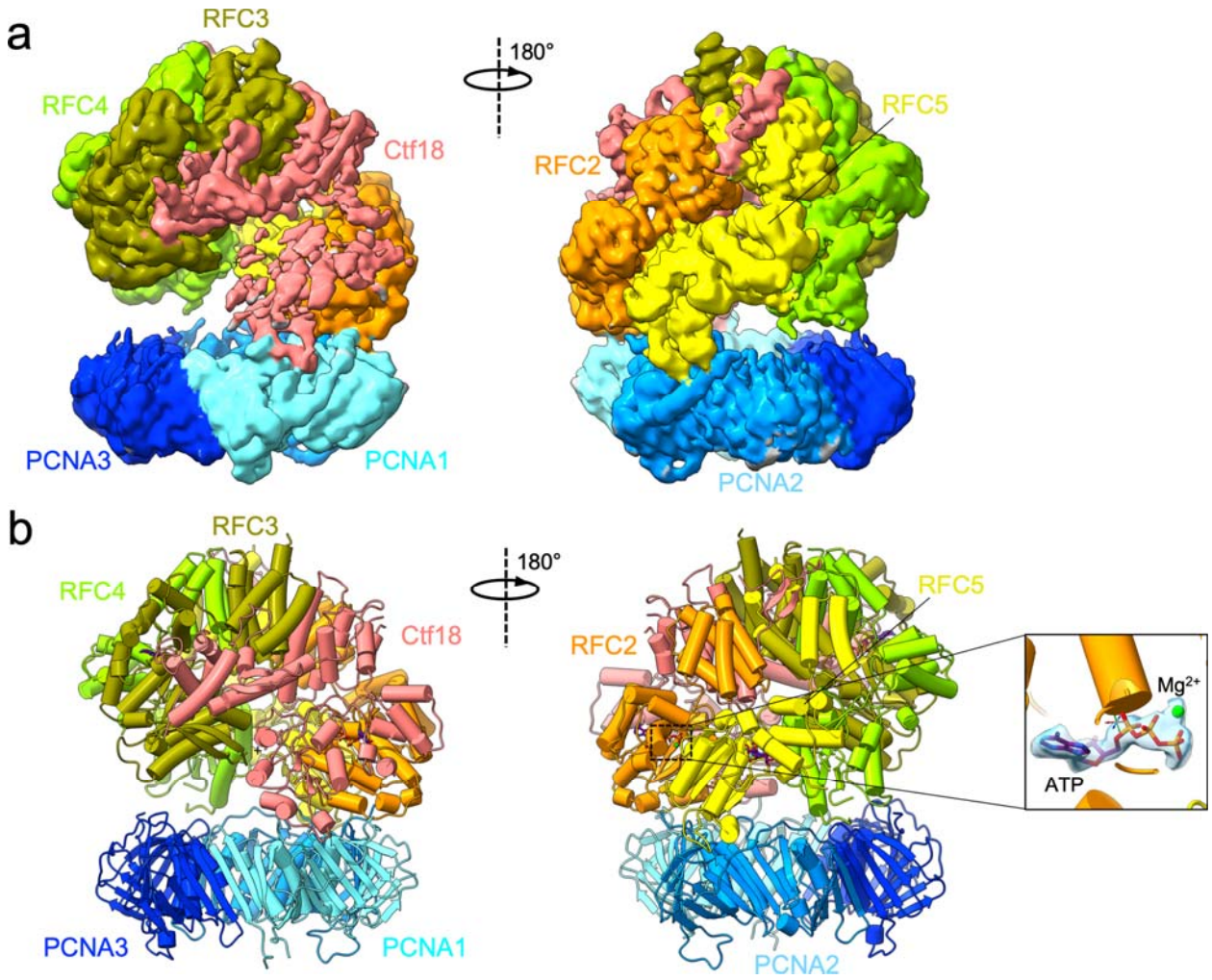


**Figure 5**. ***Cryo-EM structure of the human CTF18-RFC–PCNA complex in the presence of ATP and $Mg^{2+}$.*** **a)** Two views of the Cryo-EM map, coloured by subunits. **b)** Molecular model in ribbon representation. The inset shows a map and model of the ATP molecule bound to the RFC2 subunit, with a discernible $Mg^{2+}$ ion.

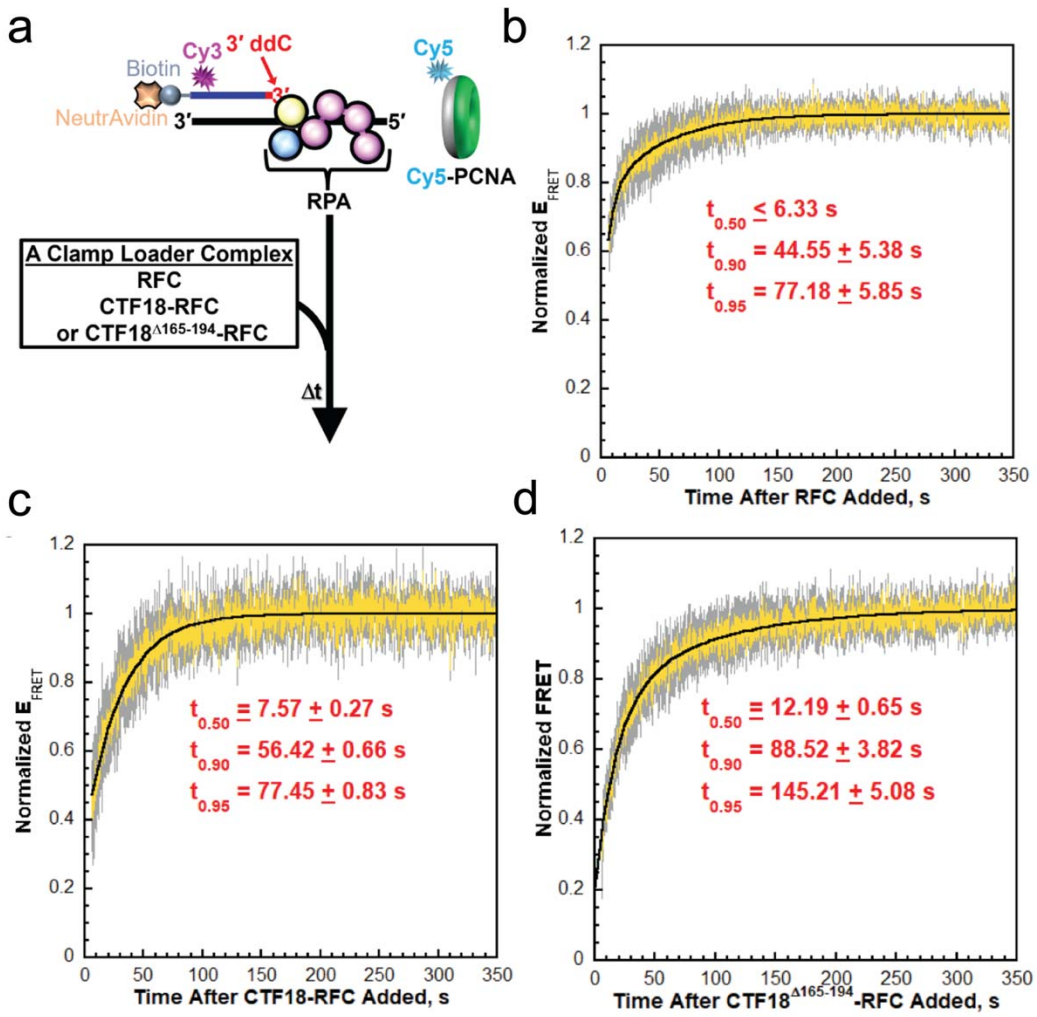


**Figure 6**. ***FRET assays to monitor loading of PCNA onto P/T junctions by human clamp loader complexes***. **a)** Schematic representation of the FRET pair and experiment to monitor loading of Cy5-PCNA onto 5′ddPCy3/T DNA substrates engaged by RPA. The front and back faces of PCNA are displayed in green and grey, respectively. When loaded onto a 5′ddPCy3/T DNA substrate, the Cy5 label on the back face of PCNA is oriented towards the Cy3 label near the blunt duplex end of the 5′ddPCy3/T DNA substrate, yielding a FRET signal **b-d)** Data. Each normalized $E_{FRET}$ trace is the mean of at least three independent traces with the S.E.M. shown in grey.

Each respective trace is fit to its corresponding minimal kinetic model and the times required for the trace to reach 50% ($t_{0.50}$), 90%, ($t_{0.90}$), and 95% ($t_{0.95}$) of the maximal value (i.e., 1.0) are reported. Data for loading of PCNA by RFC, CTF18, and CTF18$^{\Delta 165-194}$-RFC are displayed in panels **b**, **c**, and **d**, respectively.

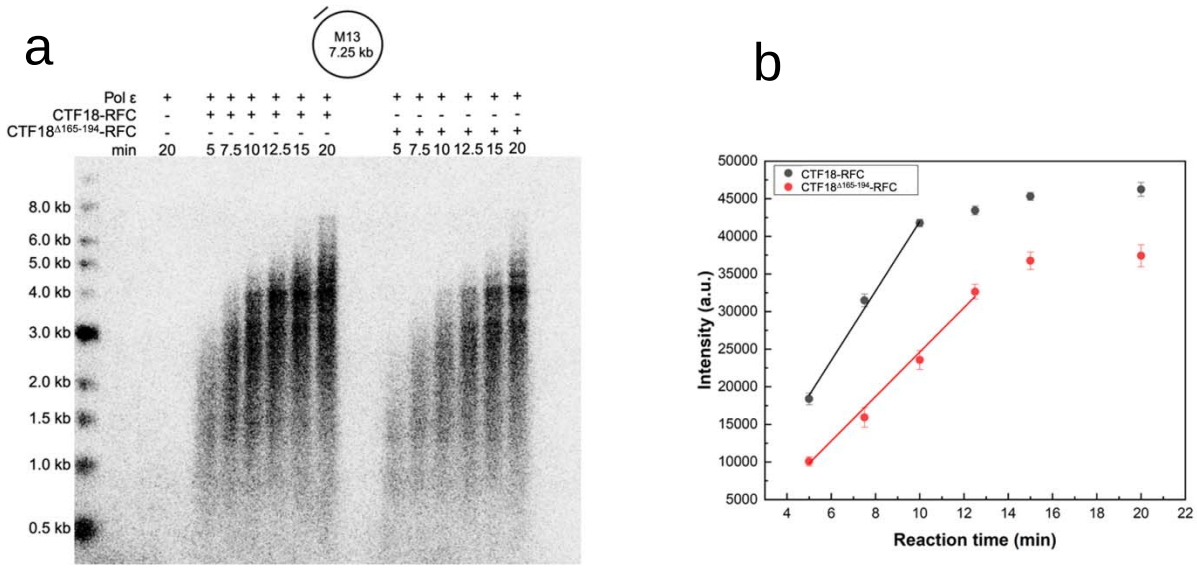


**Figure 7.** ***Primer extension assay with Pol ε and CTF18-RFC WT or CTF18$^{\Delta 165\text{-}194}$-RFC.*** **a)** Time course reactions on M13mp18 single-strand DNA with 40 nM wildtype CTF18-RFC or CTF18$^{\Delta 165\text{-}194}$-RFC. Reactions were performed as described in Materials and Methods. **b)** Quantification of the band intensities from the primer extension assay shows that the rate of increase in intensity, derived from the initial linear portion of the reaction time before saturation, is 4142 ± 95 a.u./min for CTF18-RFC and 2389 ± 143 a.u./min for CTF18$^{\Delta 165\text{-}194}$-RFC. This indicates that the mutant slows Pol ε synthesis by 42%. The experiment was conducted three times. Dots in **b)** represent mean values from the three replicas.

a

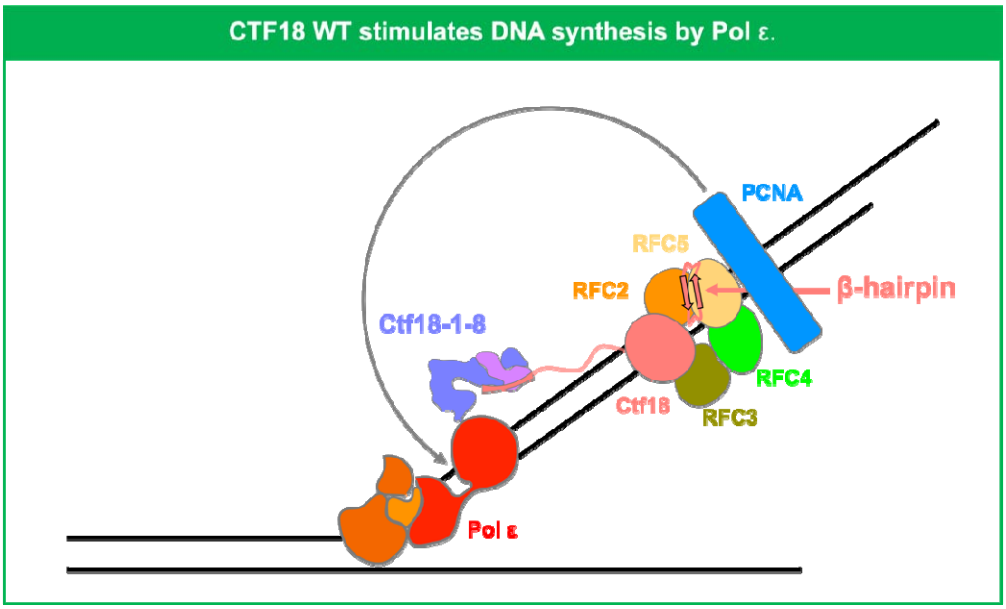


b

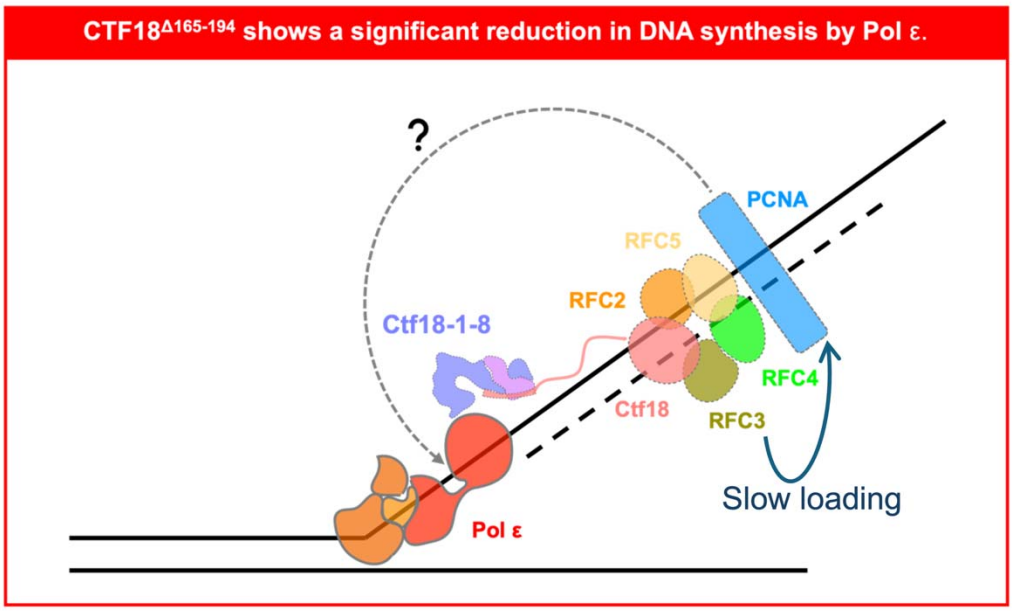


**Figure 8.** ***Deletion of the N-terminal β-hairpin in the Ctf18 large subunit slows down PCNA loading and reduces DNA synthesis by Pol ε.*** **a)** The structure of the RFC module of CTF18-RFC is stabilized by the presence of a β-hairpin in the Ctf18 subunit (amino acids 165-194). Thus, wild type CTF18-RFC loads PCNA onto DNA

efficiently and stimulates DNA synthesis by Pol ε interacting with the polymerase. **b)** The stability of the CTF18-RFC–PCNA complex is diminished by the deletion of the β-hairpin. Consequently, a CTF18-RFC deletion mutant lacking the β-hairpin (CTF18$^{\Delta 165-194}$-RFC) shows slower loading of PCNA and lower activity in stimulating primer synthesis by Pol ε.

# References


1. Hubscher U, Maga G, Spadari S. Eukaryotic DNA polymerases. Annu Rev Biochem. 2002;71:133-63.
2. Choe KN, Moldovan GL. Forging Ahead through Darkness: PCNA, Still the Principal Conductor at the Replication Fork. Mol Cell. 2017;65(3):380-92.
3. Moldovan GL, Pfander B, Jentsch S. PCNA controls establishment of sister chromatid cohesion during S phase. Mol Cell. 2006;23(5):723-32.
4. Indiani C, O'Donnell M. The replication clamp-loading machine at work in the three domains of life. Nat Rev Mol Cell Biol. 2006;7(10):751-61.
5. Kelch BA, Makino DL, O'Donnell M, Kuriyan J. Clamp loader ATPases and the evolution of DNA replication machinery. Bmc Biology. 2012;10.
6. Kang MS, Ryu E, Lee SW, Park J, Ha NY, Ra JS, et al. Regulation of PCNA cycling on replicating DNA by RFC and RFC-like complexes. Nature Communications. 2019;10.
7. Jeruzalmi D, O'Donnell M, Kuriyan J. Crystal structure of the processivity clamp loader gamma (γ) complex of DNA polymerase III. Cell. 2001;106(4):429-41.
8. Bowman GD, O'Donnell M, Kuriyan J. Structural analysis of a eukaryotic sliding DNA clamp-clamp loader complex. Nature. 2004;429(6993):724-30.
9. Kazmirski SL, Podobnik M, Weitze TF, O'Donnelll M, Kuriyan J. Structural analysis of the inactive state of the DNA polymerase clamp-loader complex. Proceedings of the National Academy of Sciences of the United States of America. 2004;101(48):16750-5.
10. Gaubitz C, Liu XC, Magrino J, Stone NP, Landeck J, Hedglin M, et al. Structure of the human clamp loader reveals an autoinhibited conformation of a substrate-bound AAA plus switch. Proceedings of the National Academy of Sciences of the United States of America. 2020;117(38):23571-80.
11. Gaubitz C, Liu XC, Pajak J, Stone NP, Hayes JA, Demo G, et al. Cryo-EM structures reveal high-resolution mechanism of a DNA polymerase sliding clamp loader. Elife. 2022;11.
12. Schrecker M, Castaneda JC, Devbhandari S, Kumar C, Remus D, Hite RK. Multistep loading of a DNA sliding clamp onto DNA by replication factor C. Elife. 2022;11.
13. Turner J, Hingorani MM, Kelman Z, O'Donnell M. The internal workings of a DNA polymerase clamp-loading machine. EMBO J. 1999;18(3):771-83.
14. Gomes XV, Schmidt SL, Burgers PM. ATP utilization by yeast replication factor C. II. Multiple stepwise ATP binding events are required to load proliferating cell nuclear antigen onto primed DNA. J Biol Chem. 2001;276(37):34776-83.
15. Chen S, Levin MK, Sakato M, Zhou Y, Hingorani MM. Mechanism of ATP-driven PCNA clamp loading by S. cerevisiae RFC. J Mol Biol. 2009;388(3):431-42.
16. Simonetta KR, Kazmirski SL, Goedken ER, Cantor AJ, Kelch BA, McNally R, et al. The mechanism of ATP-dependent primer-template recognition by a clamp loader complex. Cell. 2009;137(4):659-71.
17. Kelch BA, Makino DL, O'Donnell M, Kuriyan J. How a DNA polymerase clamp loader opens a sliding clamp. Science. 2011;334(6063):1675-80.

921 18. Kelch BA. Review: The lord of the rings: Structure and mechanism of the sliding clamp
922 loader. Biopolymers. 2016;105(8):532-46.
923 19. Jeruzalmi D, O'Donnell M, Kuriyan J. Clamp loaders and sliding clamps. Curr Opin Struct
924 Biol. 2002;12(2):217-24.
925 20. Lee KY, Park SH. Eukaryotic clamp loaders and unloaders in the maintenance of genome
926 stability. Exp Mol Med. 2020;52(12):1948-58.
927 21. Mayer ML, Gygi SP, Aebersold R, Hieter P. Identification of RFC(Ctf18p, Ctf8p, Dcc1p): an
928 alternative RFC complex required for sister chromatid cohesion in S. cerevisiae. Mol Cell.
929 2001;7(5):959-70.
930 22. Naiki T, Kondo T, Nakada D, Matsumoto K, Sugimoto K. Chl12 (Ctf18) forms a novel
931 replication factor C-related complex and functions redundantly with Rad24 in the DNA
932 replication checkpoint pathway. Mol Cell Biol. 2001;21(17):5838-45.
933 23. Bylund GO, Burgers PM. Replication protein A-directed unloading of PCNA by the Ctf18
934 cohesion establishment complex. Mol Cell Biol. 2005;25(13):5445-55.
935 24. Crabbe L, Thomas A, Pantesco V, De Vos J, Pasero P, Lengronne A. Analysis of replication
936 profiles reveals key role of RFC-Ctf18 in yeast replication stress response. Nat Struct Mol Biol.
937 2010;17(11):1391-7.
938 25. Liu HW, Bouchoux C, Panarotto M, Kakui Y, Patel H, Uhlmann F. Division of Labor
939 between PCNA Loaders in DNA Replication and Sister Chromatid Cohesion Establishment. Mol
940 Cell. 2020;78(4):725-38 e4.
941 26. al-Khodairy F, Carr AM. DNA repair mutants defining G2 checkpoint pathways in
942 Schizosaccharomyces pombe. EMBO J. 1992;11(4):1343-50.
943 27. Kim J, Robertson K, Mylonas KJ, Gray FC, Charapitsa I, MacNeill SA. Contrasting effects of
944 Elg1-RFC and Ctf18-RFC inactivation in the absence of fully functional RFC in fission yeast.
945 Nucleic Acids Res. 2005;33(13):4078-89.
946 28. Bermudez VP, Lindsey-Boltz LA, Cesare AJ, Maniwa Y, Griffith JD, Hurwitz J, et al. Loading
947 of the human 9-1-1 checkpoint complex onto DNA by the checkpoint clamp loader hRad17-
948 replication factor C complex in vitro. Proc Natl Acad Sci U S A. 2003;100(4):1633-8.
949 29. Terret ME, Sherwood R, Rahman S, Qin J, Jallepalli PV. Cohesin acetylation speeds the
950 replication fork. Nature. 2009;462(7270):231-4.
951 30. Zhang J, Shi X, Li Y, Kim BJ, Jia J, Huang Z, et al. Acetylation of Smc3 by Eco1 is required
952 for S phase sister chromatid cohesion in both human and yeast. Mol Cell. 2008;31(1):143-51.
953 31. Rolef Ben-Shahar T, Heeger S, Lehane C, East P, Flynn H, Skehel M, et al. Eco1-dependent
954 cohesin acetylation during establishment of sister chromatid cohesion. Science.
955 2008;321(5888):563-6.
956 32. Unal E, Heidinger-Pauli JM, Kim W, Guacci V, Onn I, Gygi SP, et al. A molecular
957 determinant for the establishment of sister chromatid cohesion. Science. 2008;321(5888):566-
958 9.
959 33. Kubota T, Nishimura K, Kanemaki MT, Donaldson AD. The Elg1 replication factor C-like
960 complex functions in PCNA unloading during DNA replication. Mol Cell. 2013;50(2):273-80.
961 34. Stokes K, Winczura A, Song B, Piccoli G, Grabarczyk DB. Ctf18-RFC and DNA Pol form a
962 stable leading strand polymerase/clamp loader complex required for normal and perturbed
963 DNA replication. Nucleic Acids Res. 2020;48(14):8128-45.

964 35. Bermudez VP, Maniwa Y, Tappin I, Ozato K, Yokomori K, Hurwitz J. The alternative Ctf18-
965 Dcc1-Ctf8-replication factor C complex required for sister chromatid cohesion loads proliferating
966 cell nuclear antigen onto DNA. Proc Natl Acad Sci U S A. 2003;100(18):10237-42.
967 36. Fujisawa R, Ohashi E, Hirota K, Tsurimoto T. Human CTF18-RFC clamp-loader complexed
968 with non-synthesising DNA polymerase epsilon efficiently loads the PCNA sliding clamp. Nucleic
969 Acids Res. 2017;45(8):4550-63.
970 37. Grabarczyk DB, Silkenat S, Kisker C. Structural Basis for the Recruitment of Ctf18-RFC to
971 the Replisome. Structure. 2018;26(1):137-44 e3.
972 38. Jones ML, Baris Y, Taylor MRG, Yeeles JTP. Structure of a human replisome shows the
973 organisation and interactions of a DNA replication machine. EMBO J. 2021;40(23):e108819.
974 39. Langston LD, Zhang D, Yurieva O, Georgescu RE, Finkelstein J, Yao NY, et al. CMG helicase
975 and DNA polymerase epsilon form a functional 15-subunit holoenzyme for eukaryotic leading-
976 strand DNA replication. Proc Natl Acad Sci U S A. 2014;111(43):15390-5.
977 40. Yeeles JTP, Janska A, Early A, Diffley JFX. How the Eukaryotic Replisome Achieves Rapid
978 and Efficient DNA Replication. Mol Cell. 2017;65(1):105-16.
979 41. Chilkova O, Stenlund P, Isoz I, Stith CM, Grabowski P, Lundstrom EB, et al. The eukaryotic
980 leading and lagging strand DNA polymerases are loaded onto primer-ends via separate
981 mechanisms but have comparable processivity in the presence of PCNA. Nucleic Acids Res.
982 2007;35(19):6588-97.
983 42. Shahid T, Danazumi AU, Tehseen M, Alhudhali L, Clark AR, Savva CG, et al. Structural
984 dynamics of DNA unwinding by a replicative helicase. Nature. 2025;641(8061):240-9.
985 43. Punjani A, Rubinstein JL, Fleet DJ, Brubaker MA. cryoSPARC: algorithms for rapid
986 unsupervised cryo-EM structure determination. Nat Methods. 2017;14(3):290-6.
987 44. Punjani A, Fleet DJ. 3D variability analysis: Resolving continuous flexibility and discrete
988 heterogeneity from single particle cryo-EM. J Struct Biol. 2021;213(2):107702.
989 45. Jumper J, Evans R, Pritzel A, Green T, Figurnov M, Ronneberger O, et al. Highly accurate
990 protein structure prediction with AlphaFold. Nature. 2021;596(7873):583-9.
991 46. Cai J, Uhlmann F, Gibbs E, Flores-Rozas H, Lee CG, Phillips B, et al. Reconstitution of
992 human replication factor C from its five subunits in baculovirus-infected insect cells. Proc Natl
993 Acad Sci U S A. 1996;93(23):12896-901.
994 47. Podust VN, Tiwari N, Ott R, Fanning E. Functional interactions among the subunits of
995 replication factor C potentiate and modulate its ATPase activity. J Biol Chem.
996 1998;273(21):12935-42.
997 48. Cai J, Yao N, Gibbs E, Finkelstein J, Phillips B, O'Donnell M, et al. ATP hydrolysis catalyzed
998 by human replication factor C requires participation of multiple subunits. Proc Natl Acad Sci U S
999 A. 1998;95(20):11607-12.
1000 49. Schmidt SL, Gomes XV, Burgers PM. ATP utilization by yeast replication factor C. III. The
1001 ATP-binding domains of Rfc2, Rfc3, and Rfc4 are essential for DNA recognition and clamp
1002 loading. J Biol Chem. 2001;276(37):34784-91.
1003 50. Seybert A, Wigley DB. Distinct roles for ATP binding and hydrolysis at individual subunits
1004 of an archaeal clamp loader. EMBO J. 2004;23(6):1360-71.
1005 51. Sakato M, O'Donnell M, Hingorani MM. A central swivel point in the RFC clamp loader
1006 controls PCNA opening and loading on DNA. J Mol Biol. 2012;416(2):163-75.

1007 52. Norris JL, Rogers LO, Pytko KG, Dannenberg RL, Perreault S, Kaushik V, et al. Replication
1008 protein A dynamically re-organizes on primer/template junctions to permit DNA polymerase
1009 delta holoenzyme assembly and initiation of DNA synthesis. Nucleic Acids Res.
1010 2024;52(13):7650-64.
1011 53. Norris JL, Hedglin M. Direct, ensemble FRET approaches to monitor transient state
1012 kinetics of human DNA polymerase delta holoenzyme assembly and initiation of DNA synthesis.
1013 Methods Enzymol. 2024;705:271-309.
1014 54. Hedglin M, Benkovic SJ. Replication Protein A Prohibits Diffusion of the PCNA Sliding
1015 Clamp along Single-Stranded DNA. Biochemistry. 2017;56(13):1824-35.
1016 55. Liu J, Zhou Y, Hingorani MM. Linchpin DNA-binding residues serve as go/no-go controls
1017 in the replication factor C-catalyzed clamp-loading mechanism. J Biol Chem.
1018 2017;292(38):15892-906.
1019 56. He Q, Wang F, O'Donnell ME, Li H. Cryo-EM reveals a nearly complete PCNA loading
1020 process and unique features of the human alternative clamp loader CTF18-RFC. Proc Natl Acad
1021 Sci U S A. 2024;121(18):e2319727121.
1022 57. Henricksen LA, Umbricht CB, Wold MS. Recombinant replication protein A: expression,
1023 complex formation, and functional characterization. J Biol Chem. 1994;269(15):11121-32.
1024 58. Hedglin M, Perumal SK, Hu Z, Benkovic S. Stepwise assembly of the human replicative
1025 polymerase holoenzyme. Elife. 2013;2:e00278.
1026 59. Li M, Sengupta B, Benkovic SJ, Lee TH, Hedglin M. PCNA Monoubiquitination Is
1027 Regulated by Diffusion of Rad6/Rad18 Complexes along RPA Filaments. Biochemistry.
1028 2020;59(49):4694-702.
1029 60. Zheng SQ, Palovcak E, Armache JP, Verba KA, Cheng Y, Agard DA. MotionCor2:
1030 anisotropic correction of beam-induced motion for improved cryo-electron microscopy. Nat
1031 Methods. 2017;14(4):331-2.
1032 61. Rohou A, Grigorieff N. CTFFIND4: Fast and accurate defocus estimation from electron
1033 micrographs. J Struct Biol. 2015;192(2):216-21.
1034 62. Kimanius D, Dong L, Sharov G, Nakane T, Scheres SHW. New tools for automated cryo-
1035 EM single-particle analysis in RELION-4.0. Biochem J. 2021;478(24):4169-85.
1036 63. Bepler T, Morin A, Rapp M, Brasch J, Shapiro L, Noble AJ, et al. Positive-unlabeled
1037 convolutional neural networks for particle picking in cryo-electron micrographs. Nat Methods.
1038 2019;16(11):1153-60.
1039 64. Kelley LA, Mezulis S, Yates CM, Wass MN, Sternberg MJ. The Phyre2 web portal for
1040 protein modeling, prediction and analysis. Nat Protoc. 2015;10(6):845-58.
1041 65. Emsley P, Lohkamp B, Scott WG, Cowtan K. Features and development of Coot. Acta
1042 Crystallogr D Biol Crystallogr. 2010;66(Pt 4):486-501.
1043 66. Croll TI. ISOLDE: a physically realistic environment for model building into low-resolution
1044 electron-density maps. Acta Crystallogr D Struct Biol. 2018;74(Pt 6):519-30.
1045 67. Adams PD, Afonine PV, Bunkoczi G, Chen VB, Davis IW, Echols N, et al. PHENIX: a
1046 comprehensive Python-based system for macromolecular structure solution. Acta Crystallogr D
1047 Biol Crystallogr. 2010;66(Pt 2):213-21.